



## Refractory high-entropy alloys fabricated by powder metallurgy: Progress, challenges and opportunities



Baoguang Zhang<sup>a,b</sup>, Yuanping Huang<sup>a</sup>, Zhenyu Dou<sup>a</sup>, Jian Wang<sup>a,\*</sup>, Zhifu Huang<sup>b,\*\*</sup>

<sup>a</sup> State Key Laboratory of Porous Metal Materials, Northwest Institute for Nonferrous Metal Research, Xi'an, 710016, PR China

<sup>b</sup> State Key Laboratory for Mechanical Behavior of Materials, School of Materials Science and Engineering, Xi'an Jiaotong University, Xi'an, 710016, PR China

### ARTICLE INFO

#### Keywords:

Refractory high-entropy alloys  
Fabrication  
Powder metallurgy  
Property  
Powder densification

### ABSTRACT

Refractory high-entropy alloys, which involve the mixing of four or more refractory metal elements in an equiatomic or near-equiatomic ratio, hold significant potential for various applications in high-temperature materials fields. This is mainly due to their stable phase structure and excellent high-temperature properties. While considerable interest has been in these alloys, most of them have been developed using melting casting technology. However, powder metallurgy has emerged as a promising alternative for further advancement in this field. It has the potential to expand the application areas and enhance the properties of these alloys. This article introduces to various techniques for fabricating pre-alloyed refractory high-entropy powders and their densification. Additionally, it reviews the methods for regulating the microstructure and properties of powder metallurgy refractory high-entropy alloys.

### 1. Introduction

Recently, high-entropy alloys (HEAs) have emerged as a prominent field of research in advanced metal materials, which are expected to break through the performance limits of new structural materials with novel concepts of component design. HEAs are usually composed of four or more principal elements with equal or similar atomic fractions, which show four core effects, namely, high entropy effect [1], hysteresis diffusion effect [2], lattice distortion effect [3] and "cocktail" effect [4]. Through reasonable composition design and preparation techniques, HEAs can develop a simple microstructure and demonstrate excellent properties, such as high hardness, high strength, resistance to high-temperature softening, as well as good wear and corrosion resistance [5].

Among HEAs, refractory high-entropy alloys (RHEAs) composed of high-melting-point elements (such as V, Nb, Ta, Mo, W, Ti, Zr, Re, Cr and Hf) have attracted special attention [6]. Due to the high melting point of constituent elements, RHEAs system also exhibits a high melting point. Consequently, these RHEAs possess exceptional properties at elevated temperatures, making them potential superalloys for industrial applications [7]. It has been reported that the NbMoTaW and VNbMoTaW

RHEAs with single body centered cubic (BCC) structure have a good work hardening ability at room temperature and stable structure at 1400 °C [8]. More surprisingly, the yield strengths of NbMoTaW and VNbMoTaW RHEAs can still maintain 405 MPa and 477 MPa, respectively, when the temperature is as high as 1600 °C [8]. This result fully proves the great application potential of RHEAs in high-temperature field. Thus the research and development of RHEAs has attracted wide attention.

The preparation of RHEAs is a great challenge since the melting points of constituent elements are relatively high and differ greatly from each other. The most commonly used preparation method is melting casting [9], mainly including vacuum arc melting, induction melting and electron beam melting. Melting has already been used to produce HEAs in the shape of rods [10], bars [11], ribbons [12] and microwires [13]. Microwire HEAs generally show a large magnetocaloric effect (MCE), which provides great possibilities for realizing high-efficiency and low-pollution magnetic refrigeration [13–15]. However, melting generally requires significantly higher temperatures, and some elements with high melting points are difficult to melt or melt atoms diffuse slowly, leading to obvious element segregation and defects such as dendrite structure, pores and residual stress on a scale of hundreds of

Peer review under responsibility of Vietnam National University, Hanoi.

\* Corresponding author.

\*\* Corresponding author.

E-mail addresses: [jwangxjtu@163.com](mailto:jwangxjtu@163.com) (J. Wang), [hzf@mail.xjtu.edu.cn](mailto:hzf@mail.xjtu.edu.cn) (Z. Huang).

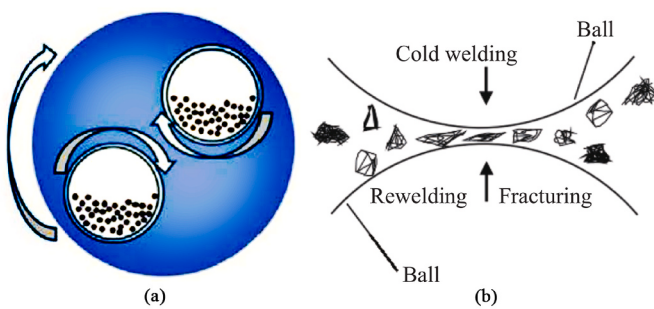


**Fig. 1.** Schematic diagrams of mechanical alloying (a) and changing process of metal powders (b). Reproduced with permission [30,33].

microns [16,17]. The grain size of RHEAs prepared by vacuum arc melting is relatively large (mostly between 100 and 300  $\mu\text{m}$  [8,18,19]), which is not conducive to exerting a grain boundary strengthening effect. Furthermore, most RHEAs possess high brittleness and hardness at room temperature, which are difficult to machine to the desired shape.

Powder metallurgy (PM) is defined as the technology of transforming powders with specific size, shape and loose density into materials with high strength, high precision and high performance. PM generally includes powder preparation, powder forming and sintering, which are near forming methods used to produce a machined part with a complicated shape [20]. Different from melting casting, PM can achieve low-temperature sintering, effectively restrain the composition segregation, prevent the formation of dendrite and multiphase precipitation, and finally obtain bulk HEAs with homogeneous phase structure [21]. Moreover, compared with melting casting, PM has obvious advantages in fabricating irregular components, which can significantly improve material utilization and reduce cost. Furthermore, the formation of HEAs with large size and homogenization is considered as key in application and PM is the promising technology to solve the above problems. Therefore, PM has become a very potential and promising choice for preparing RHEAs, which has attracted much attention from scholars from all over the world.

The goal of this paper is to review recent technological advances and achievements in refractory high-entropy alloys fabricated by powder metallurgy (PM RHEAs), to provide guidance on the scope for future research, and to have aid in the advancement and improvement of PM RHEAs technology. The focus of this paper mainly includes the fabrication and densification of pre-alloyed powders as well as the regulation of microstructure and properties in PM RHEAs.

## 2. Powder preparation technology

Powder metallurgy is a metallurgical method for alloying constituent

elements in solid state [22]. It usually includes the preparation of pre-alloyed powders (such as mechanical alloying and atomization) and subsequent sintering, or directly adopts sintering to achieve the alloying and solidification of elemental powders. The first step in any PM process is to obtain powders (including mixed elemental powders and pre-alloyed powders) suitable for the process.

At present, studies on the preparation techniques of refractory metal element (such as W, Mo, Ta, Nb and Zr) powders have been going on for many years and well developed [23–29], but it is not the focus of this paper. Therefore, this section mainly reviews the preparation techniques of pre-alloyed RHEA powders.

### 2.1. Mechanical alloying (MA)

Mechanical alloying refers to the long-term and intense collision between metal or alloy powders and grinding balls in a high-energy ball mill, resulting in repeated cold welding, fracture and rewelding of metal powders. During this process, the diffusion of atoms in powders occurs and finally fully alloyed solid solution powders can be obtained [30–32]. The schematic diagrams showing mechanical alloying and changing process of metal powders are presented in Fig. 1 [30,33].

Each component of MA powders is fully bonded between atoms to form a solid solution or compound when the milling time is long enough. MA is one of few methods capable of homogeneously mixing two or more non-mutually soluble phases [34]. Moreover, the particle size of MA powders is in the nanometer range [35–37], which improves sintering activity and reduces the temperatures required for sintering.

Kang et al. successfully fabricated WMoTaNbV alloy powders by MA using elemental W, Nb, Ta, V and Mo powders with sizes smaller than 75  $\mu\text{m}$  (Fig. 2) [38]. After milling for 6 h, the powders with BCC single-phase structure can form. The average particle size of milled powders was about 1.6  $\mu\text{m}$ . Xin et al. reported that after MA for 30 h, the V, Nb, Mo, Ta, W powders (smaller than 45  $\mu\text{m}$ ) can be mechanically alloyed into WMoTaNbV RHEA powders in a high energy shaker ball mill [39]. Besides, the size of these powders ranged from 0 to 700 nm, with an average value of only 5.9 nm (Fig. 3) [39].

Currently, many studies have been carried out on the preparation of RHEA powders by MA, and mainly focusing on the effects of milling parameters (e.g., speed and time). Wang et al. studied the impact of milling time (0–40 h) on phase type, grain size and lattice strain of MoNbTaTiV RHEA powders [40]. They found that the dissolution sequence was Ti  $\rightarrow$  V  $\rightarrow$  Nb  $\rightarrow$  Mo  $\rightarrow$  Ta (Fig. 4a) [40]. When milling time was 20 h, MoNbTaTiV RHEA powders can be obtained (Fig. 4a). As the milling time increased, the grain size gradually decreased, while the lattice strain intensified (Fig. 4b) [40]. The XRD patterns were used to estimate grain size and lattice strain based on Williamson-Hall method [41]. MA led to the accumulation of deformation strain inside grains by introducing large strains and strain gradients, which in turn promoted

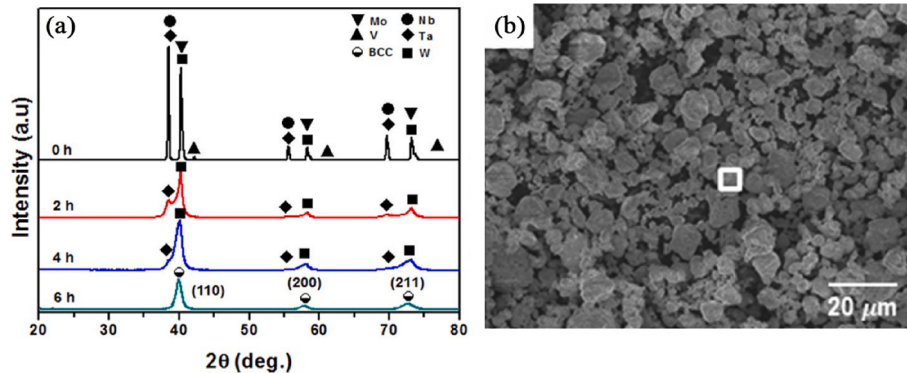


**Fig. 2.** XRD patterns of WNbMoTaV RHEA powders at different time (a) and the microstructure of WNbMoTaV RHEA powders milled for 6 h (b). Reproduced with permission [38].

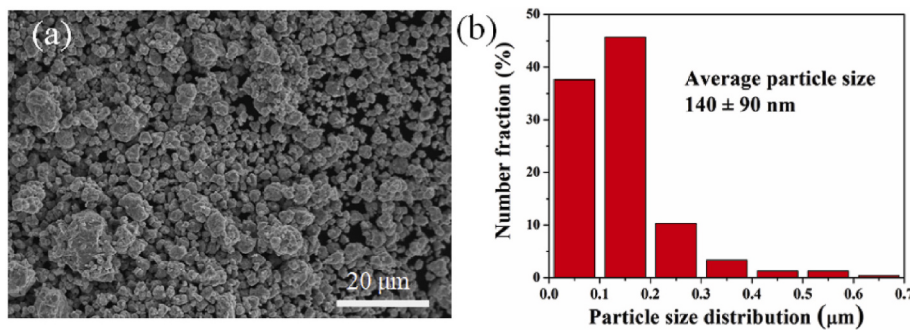


Fig. 3. SEM image (a) and particle size distribution of VNbMoTaW RHEA powders milled for 30 h (b). Reproduced with permission [39].

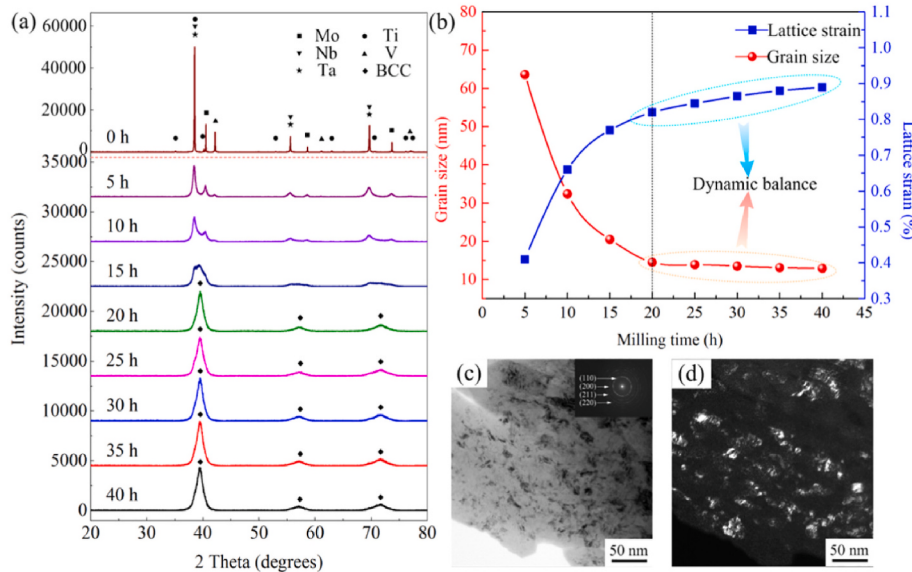


Fig. 4. XRD patterns (a), grain size and lattice strain (b), TEM bright-field image (c) and TEM dark-field image (d) of the 40 h mechanically alloyed powders. Reproduced with permission [40].

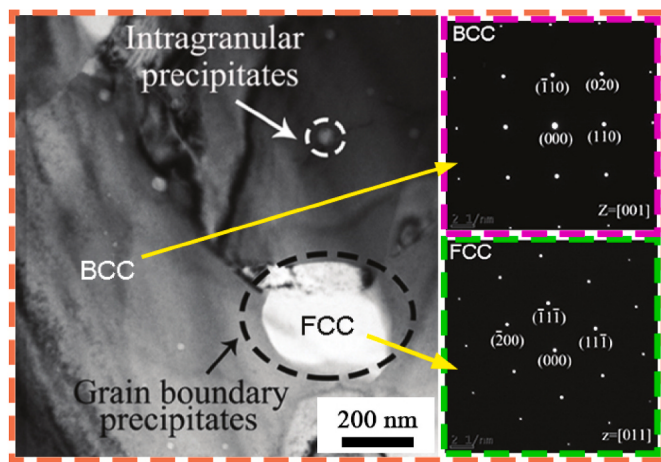


Fig. 5. TEM bright-field images of TiVNbTa alloy showing FCC precipitates.

the migration of grain boundary, increased dislocation density and ultimately resulted in the refinement of grain size. Besides, due to the large difference in size between atoms and the increase in defect density inside powders during milling, large lattice distortion was caused. With the increase of milling time, dislocations will gradually accumulate, resulting in the increase of deformation strain in the crystal, thus

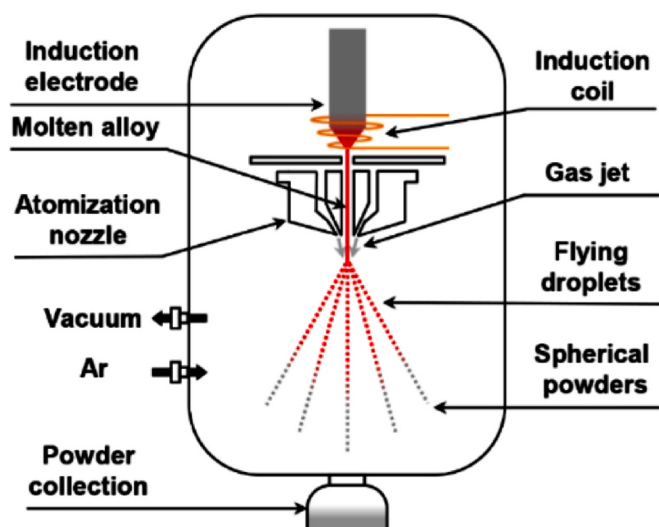


Fig. 6. Schematic diagram of the EIGA. Reproduced with permission [46].

increasing the lattice distortion. Therefore, the longer the milling time, the finer the grain size, the greater the lattice strain. Finally, the MoNbTaTiV RHEA powders with a uniform chemical distribution and an

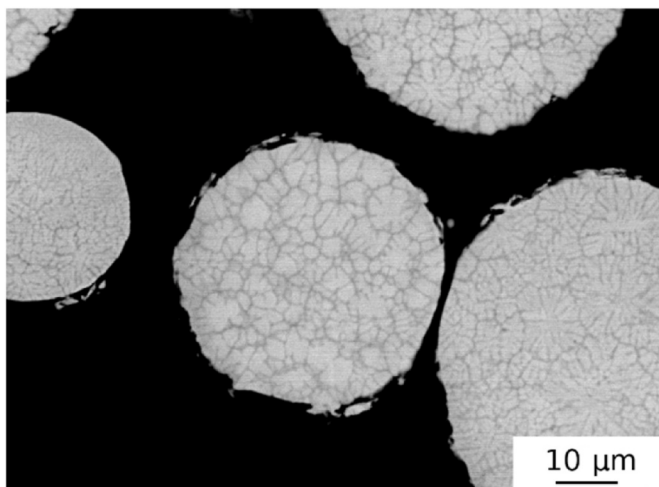


Fig. 7. Microstructure of EIGAed HfNbTaTiZr RHEA powders. Reproduced with permission [50].

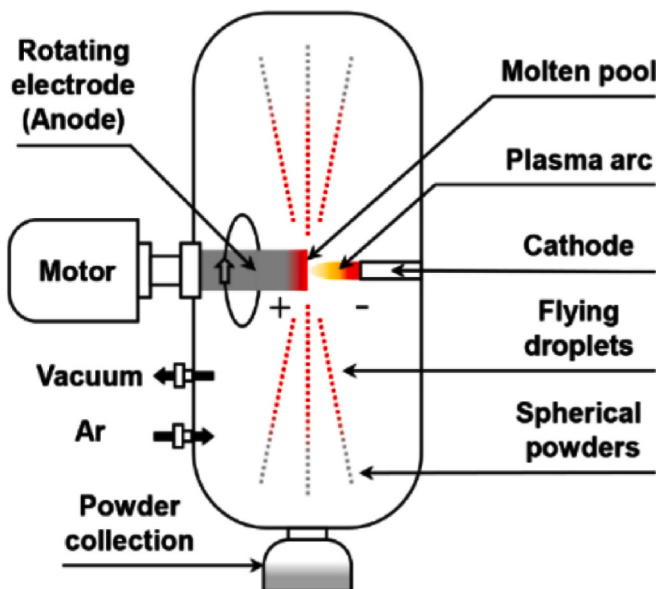


Fig. 8. Schematic of PREP apparatus principle. Reproduced with permission [46].

average grain size of less than 15 nm was obtained after 40 h milling (Fig. 4c and d) [40]. In addition, Chang et al. prepared NbVMoTa RHEA powders by MA [42]. The results showed that with the increase of milling speed, the number of effective collisions between powders increased, the phase transition energy increased, the crystallization speed accelerated, which promoted the solid solution between powders of Nb, V, Mo, Ta. Besides, the solid solution between powders was obviously enhanced as milling speed increased from 200 r/min to 400 r/min. Under the condition of 400 r/min, the solid solution between powders was more obvious as milling time prolonged to 100 h, the alloying between powders was realized, the NbVMoTa RHEA powder with single BCC structure was formed, and the particle size of powder was 30~60 nm.

Although MA can refine the particle size to nanometer level while achieving uniform alloying of RHEA powders, it still shows some disadvantages. Long et al. reported that even milling under Ar as the protecting atmosphere, the oxygen contamination of powder can occur, then the  $Ta_2VO_5$  phase will form during sintering [32]. Xin et al. found that milling of V, Nb, Mo, Ta and W powders with WC balls can lead to carbon contamination and then the formation of  $Ta_2C$  during sintering [39]. Gao et al. proved that MA to prepare TiVNbTa RHEA powders produced simultaneous contamination of C, N and O [43], and the TiC + TiO + TiN composites (marked by circles) formed after sintering (Fig. 5). According to the results of selected area electron diffraction (SAED) and

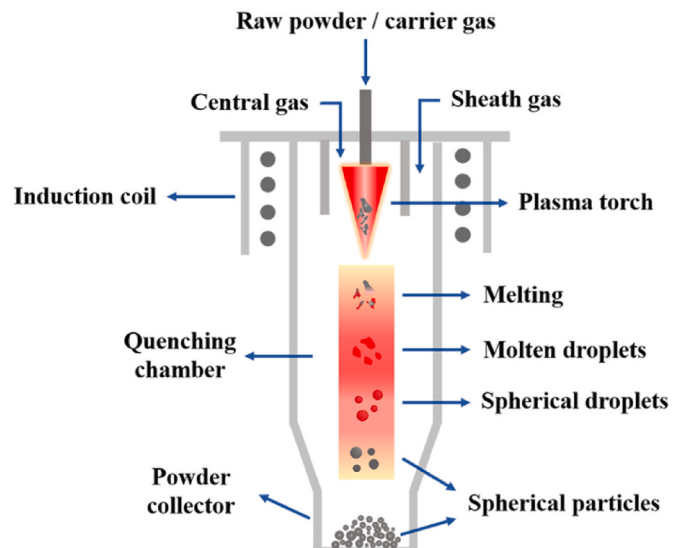


Fig. 10. Schematic diagram of plasma spheroidization system. Reproduced with permission [56].

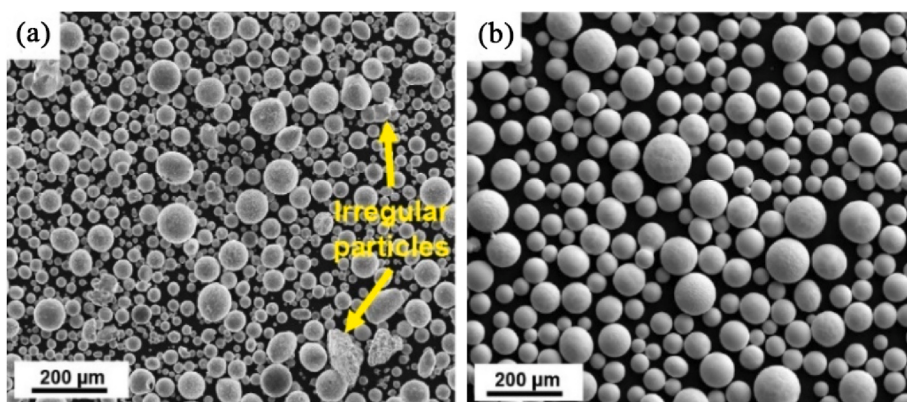
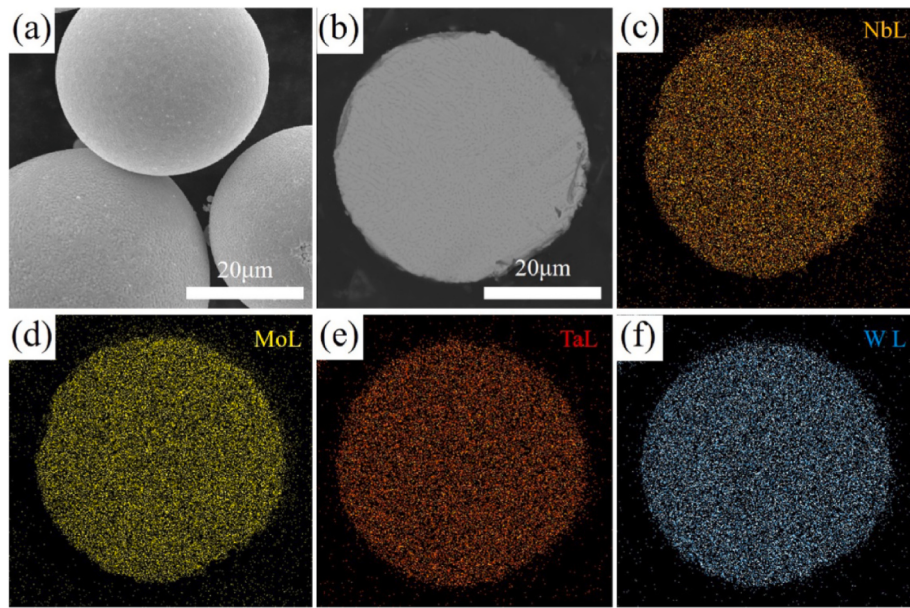
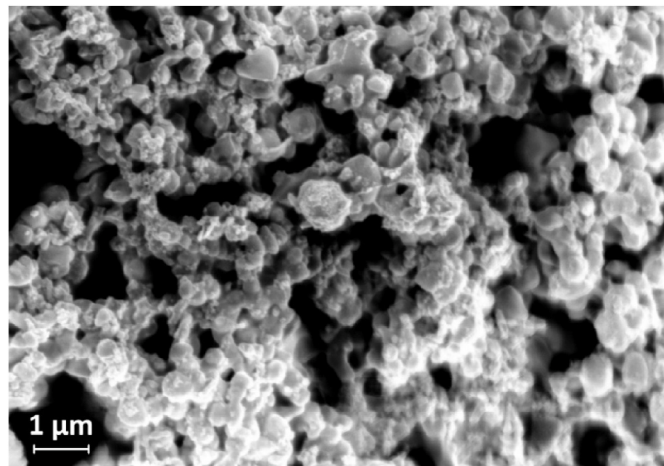


Fig. 9. SEM images of the spherical TaNbTiZr RHEA powders fabricated by EIGA (a) and PREP (b). Reproduced with permission [46].



**Fig. 11.** High magnification SEM images (a) and BSE-SEM image (b) of RHEA powders. EDS mapping for (c) Nb, (d) Mo, (e) Ta, (f) W element, respectively. Reproduced with permission [57].



**Fig. 12.** SEM micrograph of the Mo-Nb-W powders. Reproduced with permission [61].

energy dispersive spectrometer (EDS), the precipitates within BCC matrix show an FCC structure, which contain a large number of Ti and some C, N and O. Besides, lattice constants of TiN, TiC and TiO are 0.424 (PDF-#38-1420), 0.433 (PDF-#32-1283) and 0.418 (PDF-#08-0117) respectively, which are very close to the calculated lattice constant (0.431 nm) of FCC precipitates. Meanwhile, the structures of TiN, TiC and TiO in binary phase diagrams are all FCC structures at room temperature [44]. Therefore, combined with the results of EDS and TEM, it can be determined that the precipitates are TiN + TiC + TiO composites.

Overall, although mechanical alloying has the advantages of easy operation, simple equipment and high powder uniformity, it is very easy to introduce contamination of impurity elements (such as C, N, O). In addition, it also exhibits shortcomings such as long production cycle, low efficiency and high cost.

## 2.2. Electrode induction melting gas atomization (EIGA)

Electrode induction melting gas atomization is a technology that directly converts molten metal into solid powders through a fast-moving

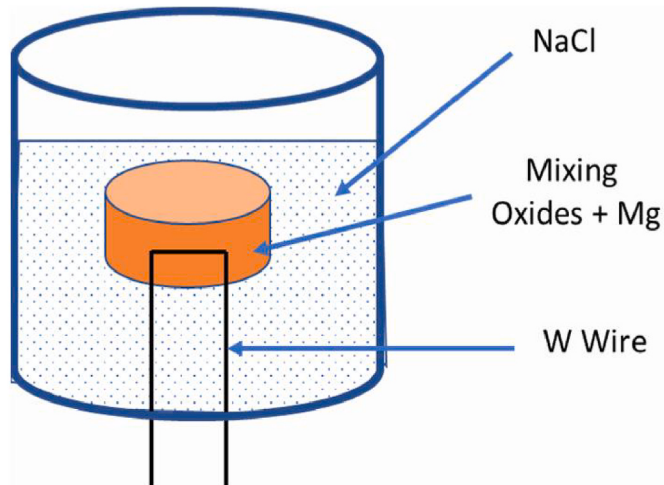


**Fig. 13.** Scheme of the SHS reactor. Reproduced with permission [62].

gas [45]. The schematic diagram of EIGA is shown in Fig. 6 [46]. During EIGA process, liquid metal is crushed into small droplets under the action of high-speed airflow, and then solidified into powder after cooling. EIGA generally shows advantages of simple process, uniform composition, high powder purity and low impurity content. And it can effectively inhibit the formation of second phase because of high cooling rate ( $1.0 \times 10^5 \sim 4.8 \times 10^6$  K/s [47]). This is due to the fact that rapid cooling can limit the movement of atoms or crystals and reduce diffusion rate of atoms, thereby the precipitation and growth of second phase can be inhibited [48].

In recent years, EIGA has been successfully used in the preparation of RHEA powders [46,49,50]. Lukac et al. prepared TaNbHfZrTi RHEA powders by EIGA, finding that the macroscopic morphology of powders was nearly spherical, and the grain size of powders was approximately 10 μm [49]. In addition, HfNbTaTiZr RHEA powders were prepared by Málek et al. via MA and EIGA respectively, and a detailed comparison was carried out [50]. The microstructure of EIGAed powder is presented in Fig. 7, showing that the size of powders was in a broad range (10–300 μm) [50]. Besides, EIGAed powders exhibited a dendritic structure

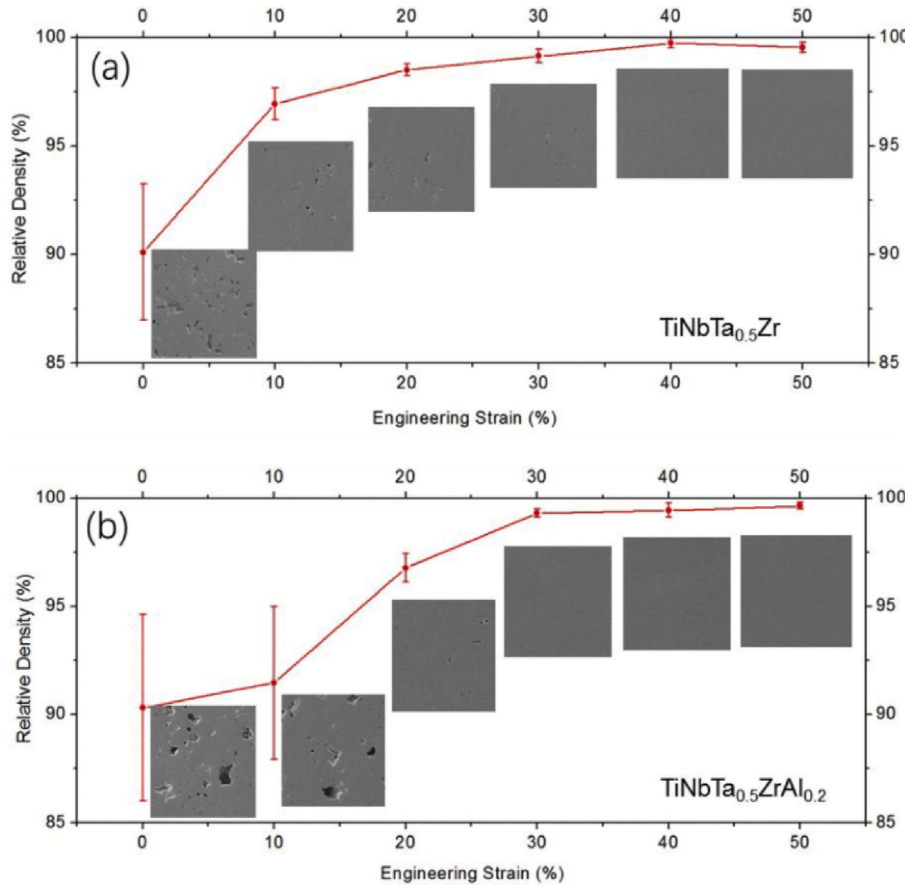


Fig. 14. Relative density of TiNbTa<sub>0.5</sub>Zr and TiNbTa<sub>0.5</sub>ZrAl<sub>0.2</sub> alloys deformed at 800 °C: (a) TiNbTa<sub>0.5</sub>Zr; (b) TiNbTa<sub>0.5</sub>ZrAl<sub>0.2</sub>. Reproduced with permission [63].

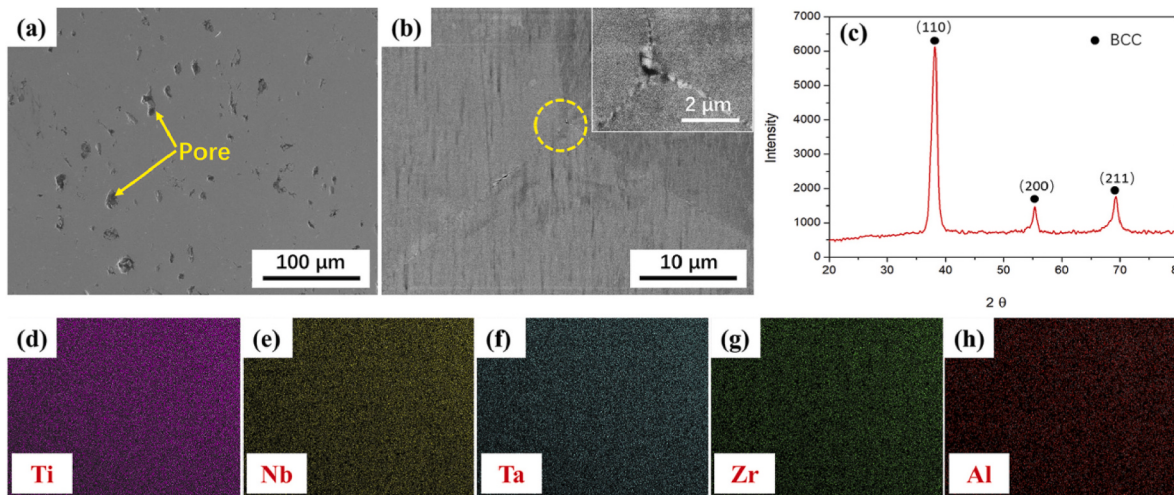


Fig. 15. Microstructure of as-sintered TiNbTa<sub>0.5</sub>ZrAl<sub>0.5</sub> alloy: (a) SE image showing residual pores; (b) BSE image around grain boundary; (c) XRD patterns; (d)~(h) elemental distribution in (b). Reproduced with permission [64].

peculiar to conventionally cast HfNbTaTiZr alloy [51]. More importantly, EIGAed powders exhibited low oxygen content (0.12 wt%), which is ten times lower than that of MA powders.

Note that, EIGA has two obvious disadvantages, namely high cost and high energy consumption. EIGA not only requires high costs of equipment, energy and material, but also has high technical requirements, thus increasing the production cost of powders. Besides, the energy used in producing powders is relatively large, and if it cannot be

effectively controlled, it will become a waste of energy.

### 2.3. Plasma rotating electrode process (PREP)

The plasma rotating electrode atomization is a centrifugal atomization method, and its schematic is shown in Fig. 8 [46]. The master alloy is processed into an electrode rod, and the high-speed rotating metal bar is continuously melted using a plasma arc as a heat source. The molten

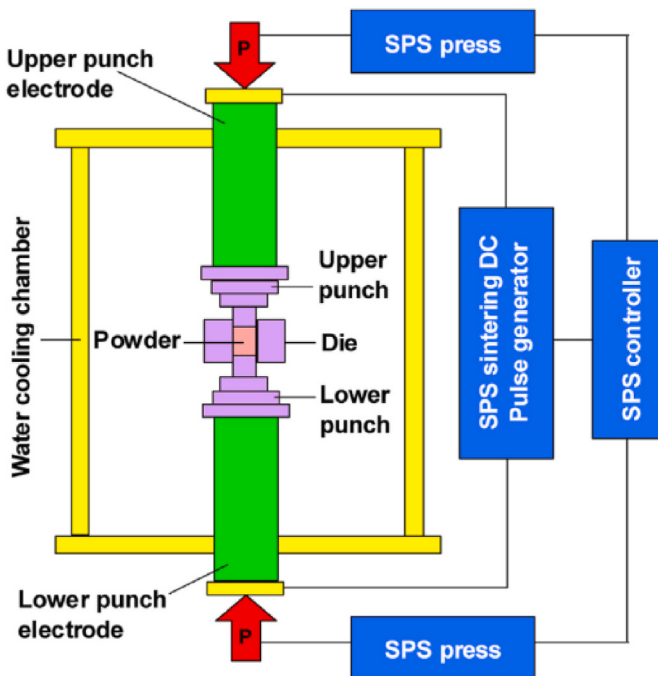


**Fig. 16.** A schematic of the SPS process. Reproduced with permission [65].

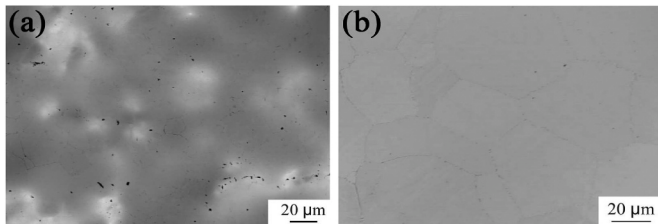


**Fig. 17.** SEM image showing the pores formed during sintering process: (a) 1500 °C; (b) 1700 °C. Reproduced with permission [66].

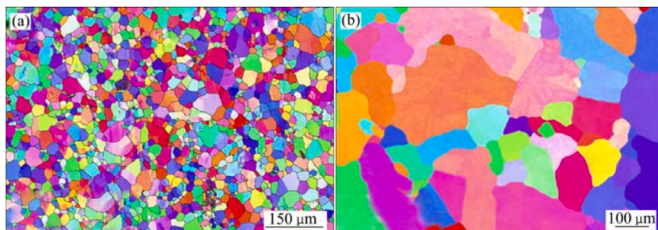


**Fig. 18.** Grain size analysis of high entropy alloys prepared through different methods: (a) SPS; (b) Arc melting. Reproduced with permission [66,67].

metal droplets on the end face of alloy rod fly out under the action of centrifugal force, then it is quickly cooled and solidified into spherical powder under the action of mixed gas (Ar and He) [46]. Compared with EIGA, powders prepared by PREP have the characteristics of higher sphericity, good fluidity, higher purity and lower oxygen content, and there is basically no situation of powder collision during the process, which reduces the formation of defects [52].

Gao et al. successfully prepared spherical TaNbTiZr REHA powders using EIGA and PREP [46]. Both the EIGAed and PREPed powders have a single-phase BCC structure and low oxygen content. Compared with EIGAed powders, PREPed powders exhibited higher sphericity and smoother surface, but presented larger particle size (Fig. 9) [46].

Moreover, theoretical calculations showed that the cooling rate of PREPed powders during the solidification process was an order of magnitude higher than that of EIGAed powders. More importantly, they proved that the PREPed powders showed a lower elemental segregation than that in the EIGAed powders.

The disadvantages such as coarse particle size, relatively high cost and low yield of fine powders prepared by PREP are the most concerned problems in the follow-up application. Besides, too many factors (e.g. electrode rod size, rotation speed, cooling gas ratio, feed speed, current size, material density and surface tension) can affect the particle size of powders [53–55], making it very difficult to control them well.

#### 2.4. Plasma spheroidization (PS)

The principle of preparing spherical metal powder by plasma spheroidization is as follows: conventional metal powder is fed into plasma torch through a carrier gas. The flying powders are rapidly heated in high-temperature plasma area, and instantly melted to form droplets. The droplets contract into a sphere under the action of surface tension, then the spherical powders are obtained via rapid cooling. The schematic diagram of PS system is presented in Fig. 10 [56].

The utilization of PS technology to prepare spherical powders mainly has following characteristics: (1) The plasma temperature is as high as 8000–10,000 K, which is enough to melt, evaporate and vaporize refractory metals, while it can not be satisfied by traditional powder preparation methods. (2) The plasma has very high energy and heat transfer efficiency, which can fully heat the powder fed into the plasma area and be melted instantly. (3) Since inert gas used as working atmosphere, no impurities are introduced during the entire preparation process, and the oxygen content of powder can be effectively reduced.

Spherical NbMoTaW RHEA powders with a uniform particle size distribution ( $d_{50} = 35.0 \mu\text{m}$ ) were prepared by Liu et al. using a novel industrial method combining spray drying and PS [57]. The EDS results showed that RHEA powders with no obvious elemental segregation were produced (Fig. 11) [57]. These indicate that PS is reliable in maintaining target composition without involving pronounced contamination. In addition, the WTaMoNbBzR RHEA powders have been successfully synthesized by Xia et al. [56,58]. The powders were obtained with a single BCC phase structure, and they possessed an average particle size of 37.5  $\mu\text{m}$ . The flow property was  $15.09 \text{ s} \cdot (50 \text{ g})^{-1}$  and apparent density was  $7.42 \text{ g cm}^{-3}$ . The nano-microhardness of these RHEA powders was measured to be 7.99 GPa, which was about 1.68 GPa higher than that of the bulky RHEA with the same composition [56].

In the existing PS technology, due to the defects of process, the spheroidization rate of powder is low, the apparent density and fluidity of powders may not reach the optimal state. Moreover, the prepared powders have the disadvantages of uneven particle size distribution and high production cost [59].

#### 2.5. Self-propagating high-temperature synthesis (SHS)

Self-propagating high-temperature synthesis is a novel material preparation technology, which can be used to prepare intermetallic compounds and composites [60]. SHS synthesizes materials based on the basic principle that chemical reactions exotherm themselves. When the local chemical reaction began, reactants are transformed into products with the approach of combustion. Compared with traditional process, SHS has the advantages of short production cycle, high output and simple process, and can greatly reduce the preparation cost.

Nanometric Mo–Nb–W powders were produced by Dine et al. through SHS, and Mg was used to reduce their oxides, in presence of sodium chloride [61]. The powders showed a backbone structure of rounded particles in the 200–800 nm range (Fig. 12) [61]. Based on the above study, a specific reactor was developed by Moser et al. to fabricate WMoTaNb RHEA powders (Fig. 13) [62]. As the reactor closed, the reduction of oxide mixtures by Mg was ignited by a heated W wire

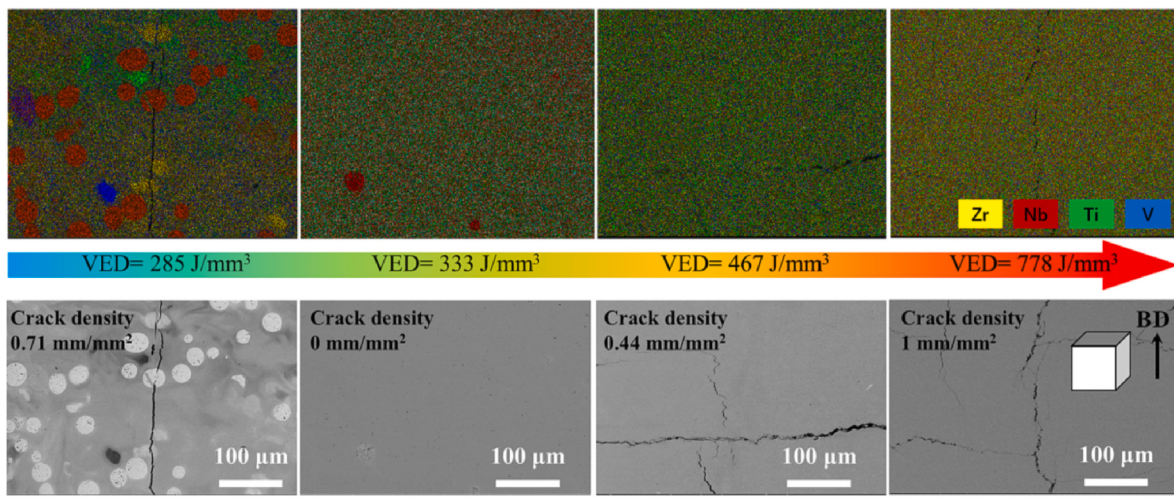


**Fig. 19.** EDS elemental mapping images and BSE images of surface morphology of the SLMed samples with different VEDs. Reproduced with permission [70].

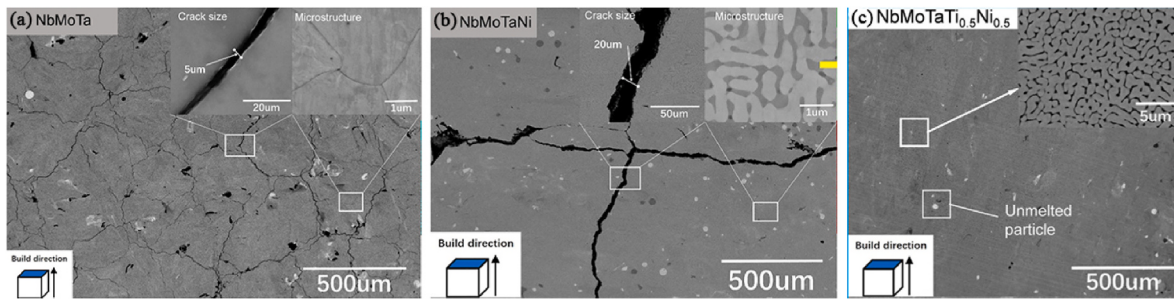


**Fig. 20.** Surface morphology of SLMed NbMoTa (a), NbMoTaNi (b) and NbMoTaTi<sub>0.5</sub>Ni<sub>0.5</sub> (c) RHEAs. Reproduced with permission [71].

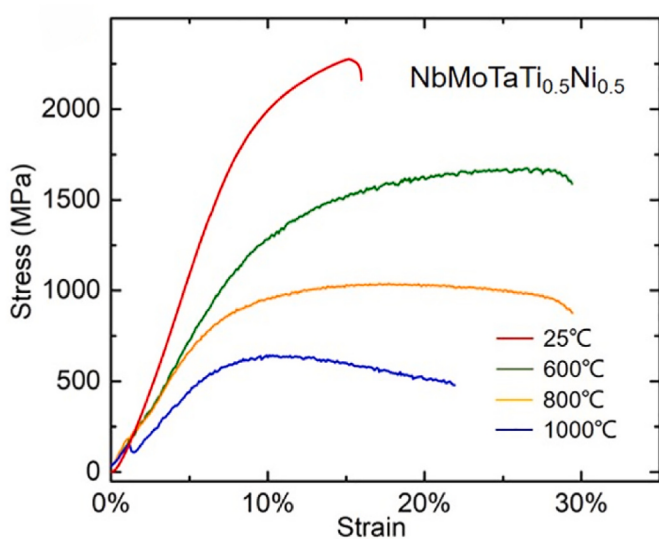


**Fig. 21.** Compressive strength of NbMoTaTi<sub>0.5</sub>Ni<sub>0.5</sub> RHEA at different temperatures. Reproduced with permission [71].

located inside the pellet. Finally, two populations of particles: larger particles of few microns (up to 20 μm) and smaller particles with a nanometer size can be obtained [62].

Although WMoTaNb RHEA powders can be synthesized by SHS, the obtained powder is not a single solid solution, but in the form of a mixture of metal phases. Therefore, the main issue for SHS route is the high number of impurities mixed with prepared RHEA powders [62].

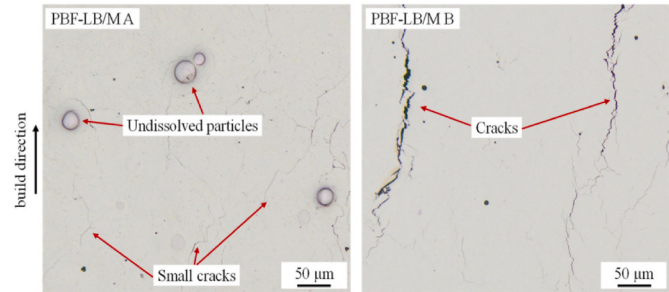


**Fig. 22.** Microsections of WMoNbTaV-samples manufactured with PBF-LB/M. Reproduced with permission [72].

### 3. Densification technology

Powder densification is a process of loosely piling or pressing raw powders, and then combining them in some way to form a dense solid. For example, during sintering process, sintering neck between powders is formed, pores are reduced and the density and mechanical properties are improved. In powder metallurgy, powder densification is a crucial step to obtain high-density bulks, including conventional sintering, spark plasma sintering (SPS) and additive manufacturing (AM).

#### 3.1. Conventional sintering

Sintering is one of the most basic processes during PM, which plays a central role in performance of final products. To put it simply, sintering is a phenomenon in which the distance between powders changes, the

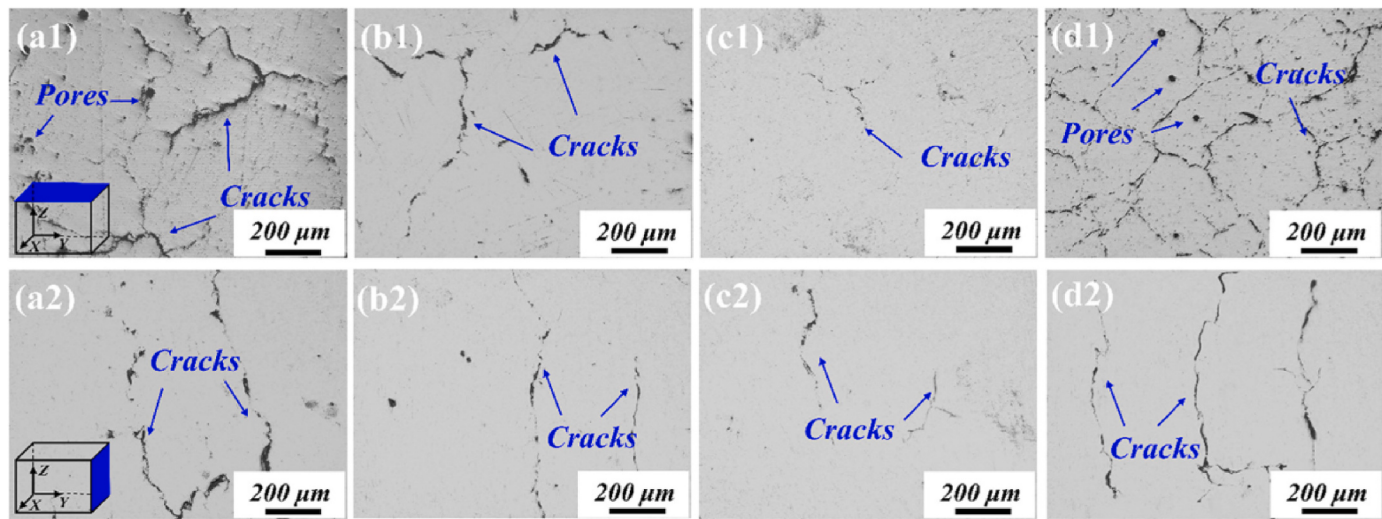


**Fig. 23.** OM images showing pores and cracks on the top surface and cross-section of VNbMoTaW RHEAs processed at (a) 800 mm/s, (b) 600 mm/s, (c) 400 mm/s and (d) 200 mm/s. Reproduced with permission [73].

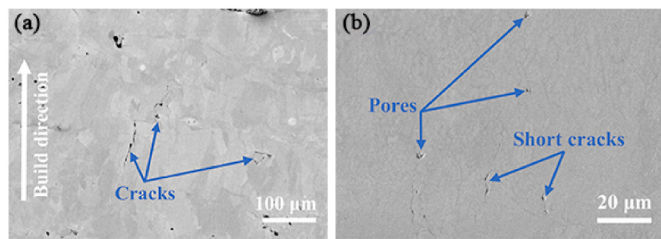


**Fig. 24.** Microstructures of the as-deposited (a) WMoTaNb and (b) WMoTaNbC RHEAs. Reproduced with permission [74].

surface area decreases and the shape changes due to the movement of atoms at high temperature. Sintering process is mainly divided into the following three stages: (1) Bonding stage. In the early stage of sintering, the original contact points or surfaces between powders transform into crystal bonds, that is, sintering necks form through atomic processes such as nucleation and crystal growth. In this stage, the grains and shape of powders remain basically unchanged, the entire sintered body does not shrink, and the change of density is not significant, but the strength and conductivity improve significantly due to the increase in powder bonding surfaces. (2) Sinter neck growth stage. A large number of atoms migrate to powder bonding surface, causing sintering neck to expand and the distance between powders to shrink, forming a continuous pore network. At the same time, as grains grow, grain boundaries move across pores, and in places swept by grain boundaries, a large number of pores disappear. Shrinkage, increase in density and strength of sintered body are main characteristics in this stage. (3) Closed pore spheroidization

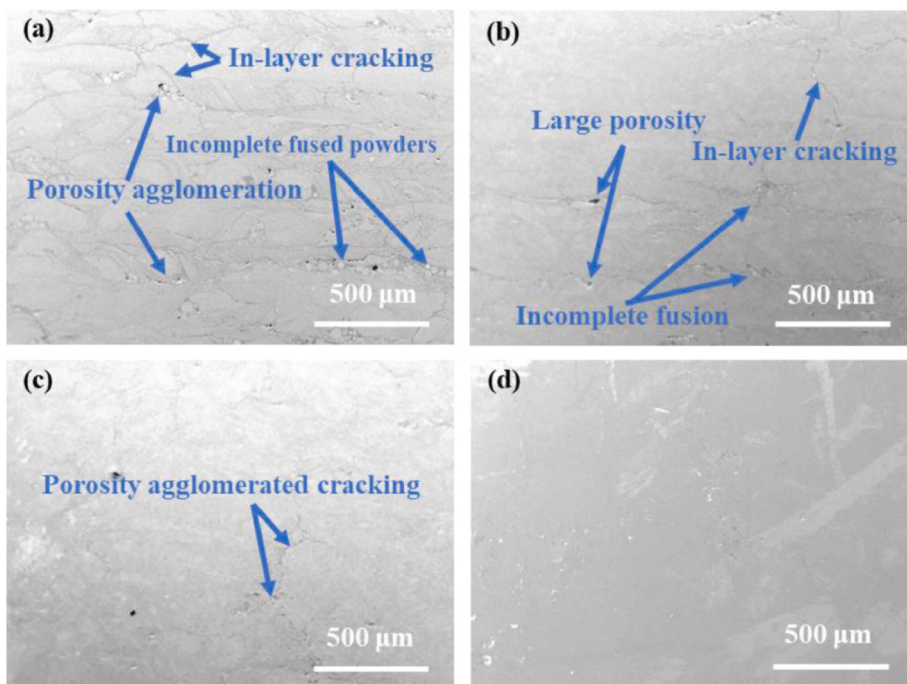


**Fig. 25.** Microstructures of as-polished surface: (a) 4.0 m/s; (b) 3.5 m/s; (c) 3.0 m/s and (d) 2.5 m/s. Reproduced with permission [75].

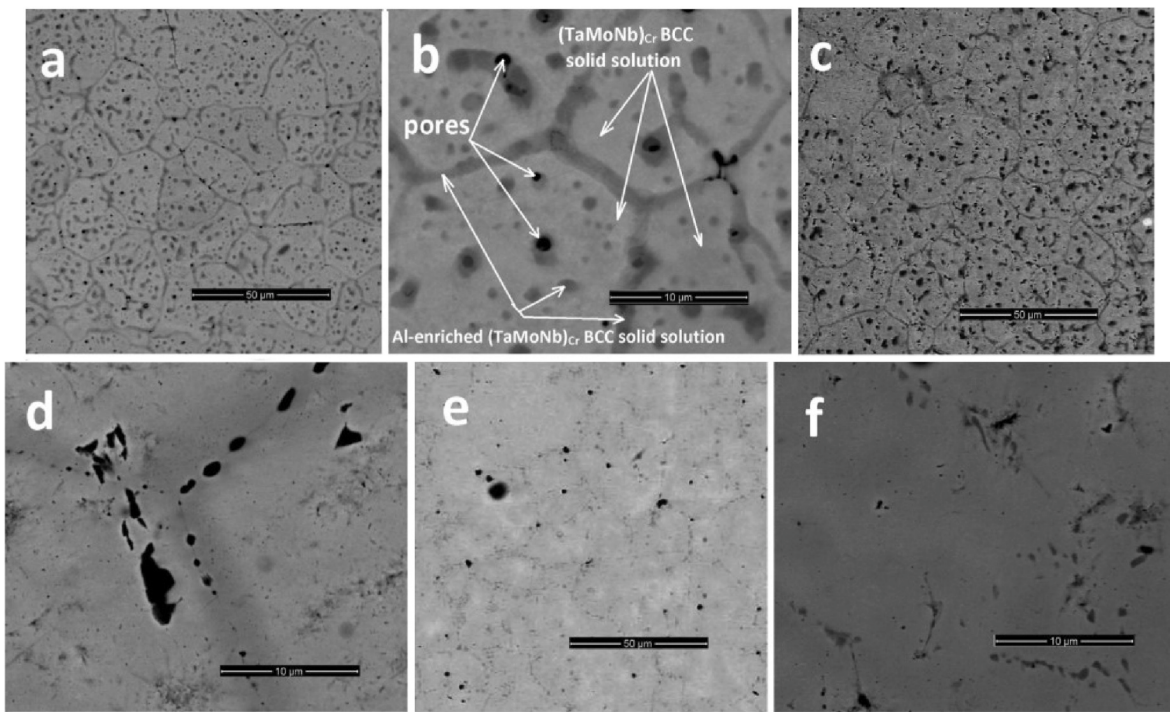


**Fig. 26.** Typical microstructures of the as-manufactured (a, b) and heat-treated samples at 1000 °C (c, d); and at 1300 °C (e, f). Reproduced with permission [76].

**Table 1**

Density  $\rho$ , melting point  $T_1$  and atomic radius  $r$  of several metal elements.

Element	$\rho/\text{g cm}^{-3}$	$T_1/^\circ\text{C}$	$r/\text{nm}$	$T_1/\rho/(\text{°C g}^{-1}\cdot\text{cm}^{-3})$
Ti	4.056	1668	0.2	411.2
Zr	6.49	1852	0.216	285.4
Hf	13.31	2227	0.159	167.3
Nb	8.57	2468	0.208	288.0
Mo	10.23	2620	0.139	256.1
Ta	16.65	2996	0.209	179.9
W	19.35	3410	0.14	176.2
V	5.96	1890	0.132	317.1
Al	2.7	660	0.143	244.4
Cr	7.19	1970	0.128	274.0

and reduction stage. When the density of sintered body reaches 90%, most pores are completely separated, the number of closed pores increases, and the pores approach a spherical shape and continue to shrink. At this stage, the entire sintered body can still shrink slowly, but this is mainly achieved by the disappearance of small pores and the reduction of pores. This stage can last for a long time, but a small number of closed pores remain and cannot be eliminated.

Cao et al. successfully prepared TiNbTaZrAl RHEA by cold isostatic pressing (CIP) at a pressure of 200 MPa and subsequent sintering at 1300 °C for 16 h in a vacuum of  $1 \times 10^{-3}$  Pa using elemental powders as raw materials [63]. The relative densities of as-sintered TiNbTa<sub>0.5</sub>Zr and TiNbTa<sub>0.5</sub>ZrAl<sub>0.2</sub> alloy were 90.3% and 90.1%, respectively [63]. Hot deformation after sintering resulted in the evolution of relative density and pores (Fig. 14) [63]. The relative density increased quickly in the initial stage, and up to 99.7% at engineering strain of 40% for TiNb-Ta<sub>0.5</sub>Zr alloy (Fig. 14a), and its density was about 7.6 g/cm<sup>3</sup>. Besides, TiNbTa<sub>0.5</sub>ZrAl<sub>0.2</sub> alloy showed a slower densification at engineering strain of 10% with a relative density only increased by 1.2%, while that of TiNbTa<sub>0.5</sub>Zr alloy was 5.8% (Fig. 14b).

Afterwards, they prepared the TiNbTa<sub>0.5</sub>ZrAl<sub>0.5</sub> HREA with a relative density of 92% and a density of 6.7 g/cm<sup>3</sup> using the same method [64]. Some residual pores can be found in the secondary electron (SE) image taken at a low magnification (Fig. 15a). The back-scattered electron (BSE) image taken around grain boundaries showed almost a single phase with very few nano-scaled precipitates (Fig. 15b). XRD results showed a single phase of BCC crystal structure in the RHEA in the as-sintered state (Fig. 15c). In addition, it can be observed that the five constituent elements distributed homogeneously, indicating that the

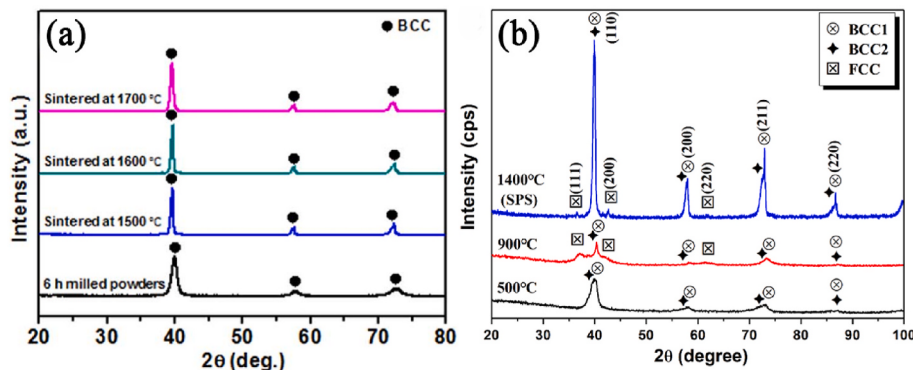


**Fig. 27.** XRD patterns of WNbMoTaV (a) and WNbMoTaVTi (b) RHEAs. Reproduced with permission [38,85].

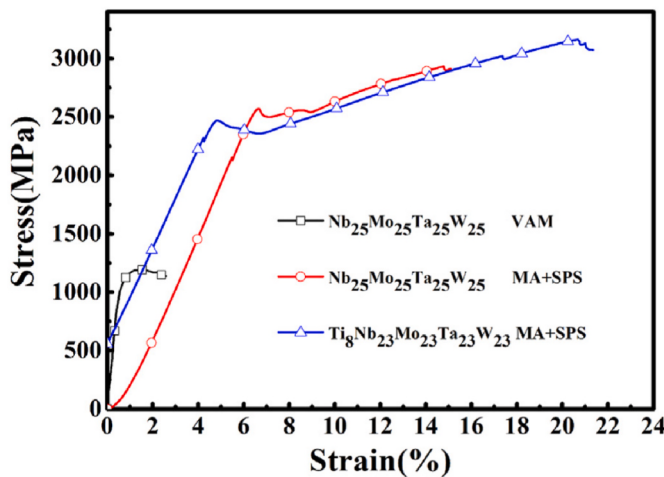


Fig. 28. Compressive engineering stress-strain curves at room temperature for Nb<sub>25</sub>Mo<sub>25</sub>Ta<sub>25</sub>W<sub>25</sub> and Ti<sub>8</sub>Nb<sub>23</sub>Mo<sub>23</sub>Ta<sub>23</sub>W<sub>23</sub> alloys. Reproduced with permission [86].

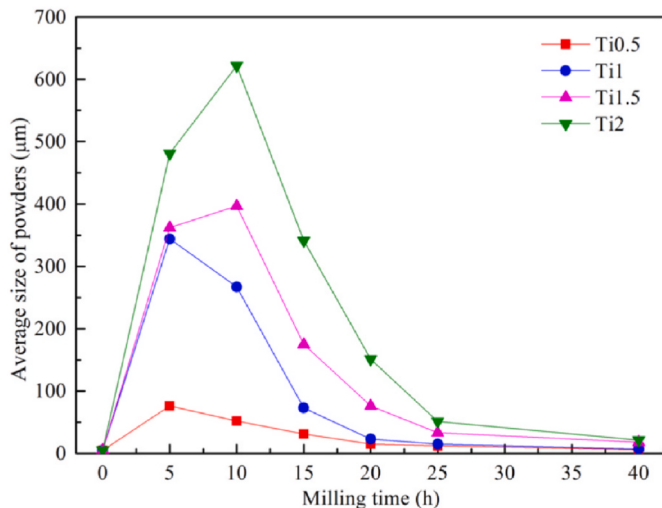


Fig. 29. Average powder sizes of the Ti<sub>x</sub>VNbMoTa RHEAs milling powders at different times. Reproduced with permission [31].

elemental powder had formed a uniform phase (Fig. 15d–h). They also proposed that further hot forging treatment after sintering can effectively improve the relative density of TiNbTa<sub>0.5</sub>ZrAl<sub>0.5</sub> HREA [64].

However, for RHEAs, although the steps of preparing pre-alloyed powders are reduced when raw materials are high-melting-point metal elemental powders, very high sintering temperature is usually needed to achieve high densification, which not only increases the production cost, but also wastes energy seriously.

### 3.2. Spark plasma sintering (SPS)

Spark plasma sintering is a pressurized sintering method which uses DC pulse current to energize the sintering directly. The heating rate and sintering temperature are controlled by adjusting DC pulse current to make powders densified quickly. The schematic of SPS process is shown in Fig. 16 [65]. Since DC pulse current passes directly through the upper and lower pressure heads and the sintered powders or graphite mold during sintering process, the heating system heats up and the heat transfer speed are very fast. Due to low sintering temperature, short sintering time and fast cooling rate, RHEAs prepared by SPS shows fine grains and can suppress the precipitation of second phase, making it easy

to obtain a single-phase alloy with a uniform structure. Consequently, SPS is currently the most commonly used preparation technology for RHEAs, combining with MA.

Guo et al. prepared TaNbVTi RHEAs through SPS. Each component element was distributed evenly without obvious segregation. After sintering at 1500 °C, small fraction of black points can be detected as pores (Fig. 17a). On the contrary, as sintering temperature increased to 1700 °C, the pores disappeared, indicating a high relative density (over 99.5 %) (Fig. 17b) [66]. Besides, this alloy showed a BCC single-phase structure with a grain size of approximately 24 μm (Fig. 18a) [66]. Alloys with similar compositions prepared by arc melting exhibited a coarse dendrite structure. The low melting point components segregated between dendrites while the high melting point components segregated within dendrites. The grain size of these alloys is much larger, about 200 μm (Fig. 18b) [67].

Lukac et al. realized the densification of milled HfNbTaTiZr powders by SPS [49]. Samples sintered at lower temperatures of 800 °C and 1000 °C contained internal porosity of 1.5% and 0.3%, respectively. At a higher sintering temperature (1200 °C), the porosity became negligible. It proved that the density of alloy increased significantly with the increase of SPS temperature. In addition, the bending strength (2500 MPa) and plasticity of sintered alloy were significantly better than those of melted alloy when the sintering temperature is higher than 1000 °C [49].

Although SPS can achieve rapid densification of RHEA powders, the size of prepared RHEA is limited. Besides, furnace for SPS will produce a lot of thermal radiation in the heating process, which will not only lead to a waste of energy, but also result in harm to operators and equipment. Besides, SPS process has high operating costs and low production efficiency, thus it is difficult to realize industrial production.

### 3.3. Additive manufacturing (AM)

Additive manufacturing, also known as 3D printing, is based on 3D model technology, which can directly form three-dimensional solid parts by stacking raw powders layer by layer. It is an emerging advanced preparation technology [68]. Compared with traditional processes, AM exhibits many advantages, including manufacturing parts with complex structures and using difficult-to-machine materials (such as Ta, W, Mo, Nb, etc.). The process offers greater design freedom and higher heating or cooling rates [69].

Recently, the V<sub>0.5</sub>Nb<sub>0.5</sub>ZrTi RHEA with a density of 6.5 g/cm<sup>3</sup> was fabricated by Zhu et al. via selective laser melting (SLM) with different volume energy density (VED) [70]. EDS elemental mapping images and BSE images of surface morphology of SLMed samples are shown in Fig. 19 [70]. The average crack density of samples decreased sharply with increasing VED from 285 J/mm<sup>3</sup> to 333 J/mm<sup>3</sup> but gradually increased when VED increased from 333 J/mm<sup>3</sup> to 778 J/mm<sup>3</sup>. In terms of mechanical properties, yield strength of crack-free SLMed sample was approximately 1450 MPa, which was nearly 1.4 times that of as-cast sample (1050 MPa) [70].

The NbMoTa, NbMoTaNi and NbMoTaTi<sub>0.5</sub>Ni<sub>0.5</sub> RHEAs have been developed by Zhang et al. by SLM [71]. The SLMed NbMoTa alloy possessed a large number of pores and micro-cracks (5~10 μm), presenting a uniform grid-like distribution (Fig. 20a). The defects were formed due to high-temperature gradient, which endowed large thermal stress to the forming surface in a small area, resulting in a tendency to crack. Simultaneously, cracking defects cannot be filled since cooling rate was greater than flow rate of molten metal, leading to the formation of cracks. The microscopic cracks and pores of NbMoTaNi alloy were obviously reduced compared to that of NbMoTa alloy (Fig. 20b). However, a macro-scale overall fracture phenomenon was also observed with the crack size of 10~30 μm. In SLMed NbMoTaTi<sub>0.5</sub>Ni<sub>0.5</sub> alloy, both macro- and micro-cracks were completely eliminated (Fig. 20c), which showed a high compressive strength of 2297 MPa at room temperature and a high-temperature (1000 °C) compressive strength of 651 MPa

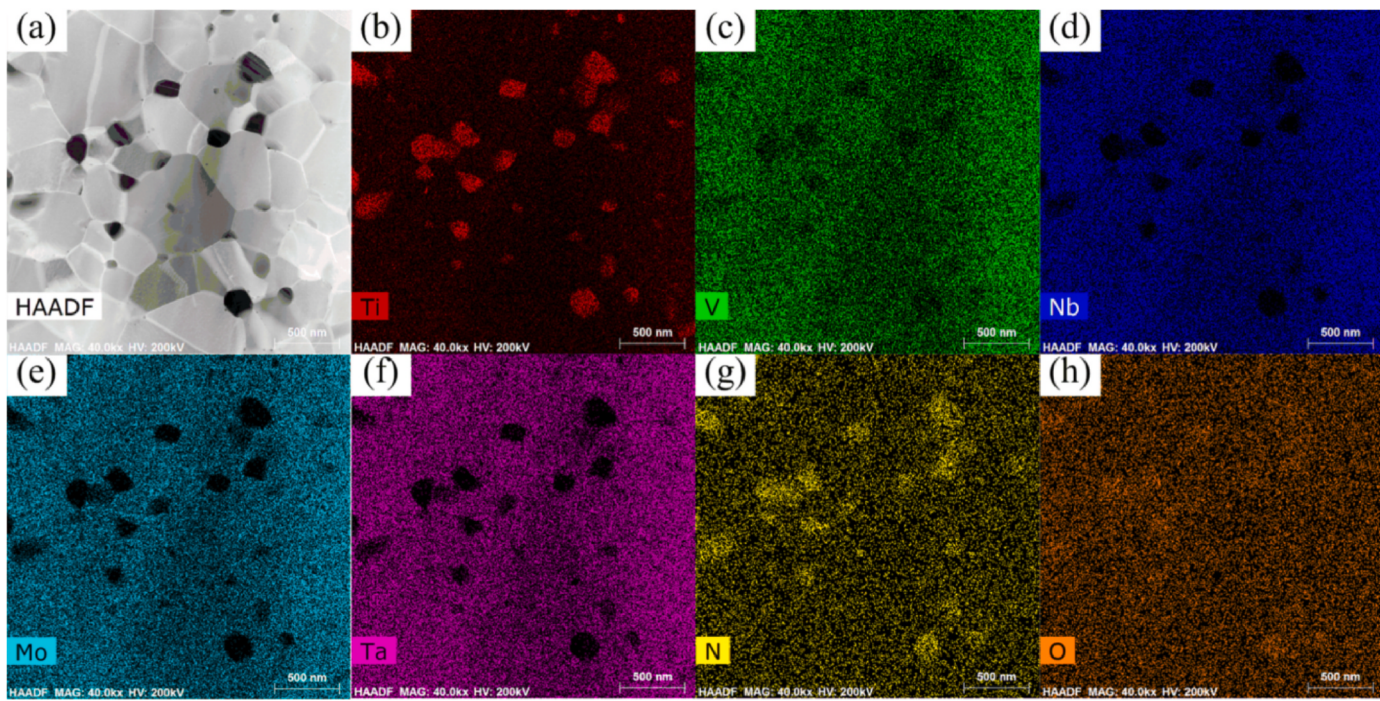


**Fig. 30.** Microstructures of the sintered  $\text{Ti}_1\text{VNbMoTa}$  RHEA: (a) HAADF image and (b–h) corresponding EDS maps of Ti, V, Nb, Mo, Ta, N and O. Reproduced with permission [31].

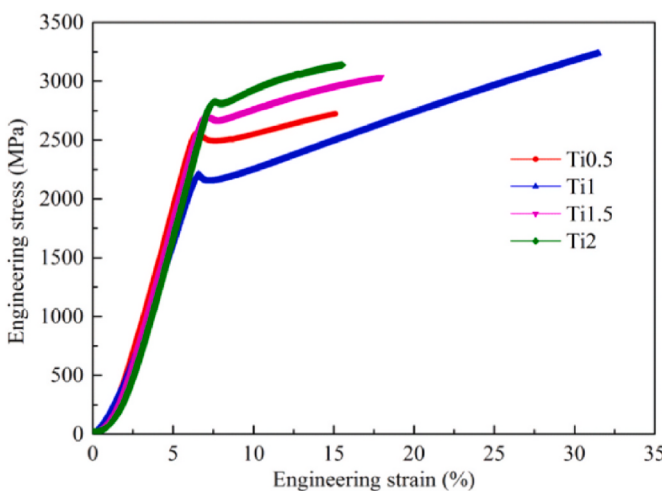


**Fig. 31.** Compressive engineering stress-strain curves of the sintered  $\text{Ti}_x\text{VNb}-\text{MoTa}$  RHEAs at room temperature. Reproduced with permission [31].

(Fig. 21) [71]. Consequently, they proposed that the addition of Ni and Ti can inhibit the formation of cracks in NbMoTa HEA prepared by SLM without affecting the mechanical properties.

Furthermore, Huber et al. demonstrated the feasibility of in-situ alloy formation of WMoTaNbV RHEA through laser powder bed fusion (PBF-LB/M) [72]. While the samples exhibited a high relative density of 99.8% in case of parameter set PBF-LB/M A and 99.5% in case of parameter set PBF-LB/M B, both samples still contained defects, as shown in Fig. 22 [72].

Gu et al. has thoroughly investigated the impact of laser scanning speed on the surface morphology, internal defect, microstructure and mechanical properties of VNbMoTaW RHEA [73]. The results showed that pores and cracks were the main sources of defects. And the manifestation of cracks was inevitable regardless of employed scanning speed (Fig. 23) [73]. Besides, VNbMoTaW RHEA specimens prepared by SLM exhibited higher compressive strength (1100–2200 MPa) than the corresponding specimens, which were prepared by the vacuum arc melting procedure.

The WMoTaNb and WMoTaNbC RHEAs was fabricated by Xiao et al. through selective electron beam melting (SEBM) [74]. The as-deposited WMoTaNb RHEA showed microstructure with significant cracks and pores (Fig. 24a). These cracks distributed along grain boundaries, coexisting with pores. In contrast, microstructure of as-deposited

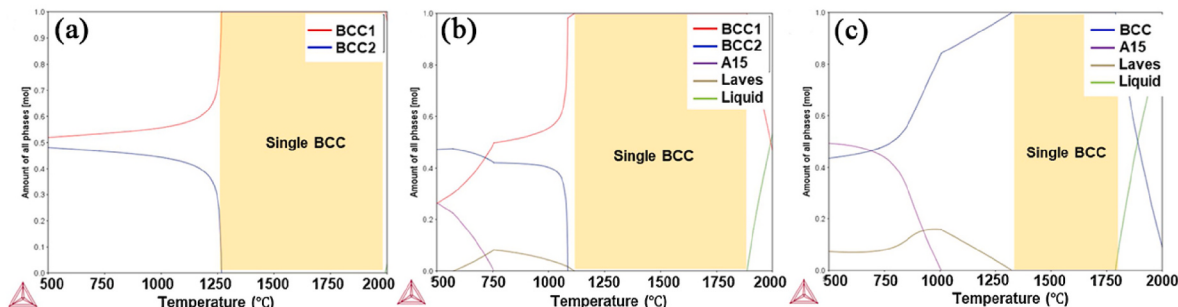


**Fig. 32.** Equilibrium phase fraction-temperature diagrams of (a)  $\text{Al}_0$ , (b)  $\text{Al}_{0.5}$ , and (c)  $\text{Al}_{1.0}$  RHEAs. Reproduced with permission [88].

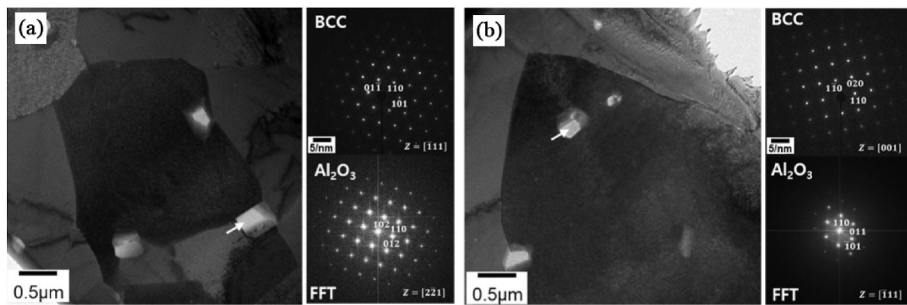


**Fig. 33.** The TEM-BF images and corresponding SAED and FFT of (a) Al<sub>0.5</sub> and (b) Al<sub>1.0</sub> RHEAs. Reproduced with permission [88].

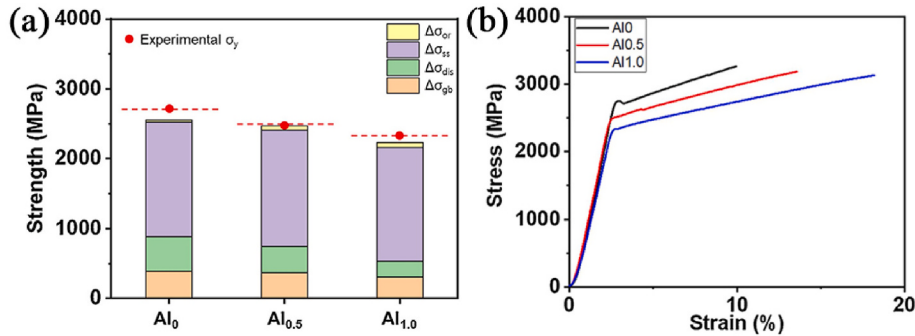


**Fig. 34.** Strengthening contributions to the yield strength (a) and compressive engineering stress and strain curves (b) of the Al<sub>0</sub>, Al<sub>0.5</sub> and Al<sub>1.0</sub> RHEAs. Reproduced with permission [88].

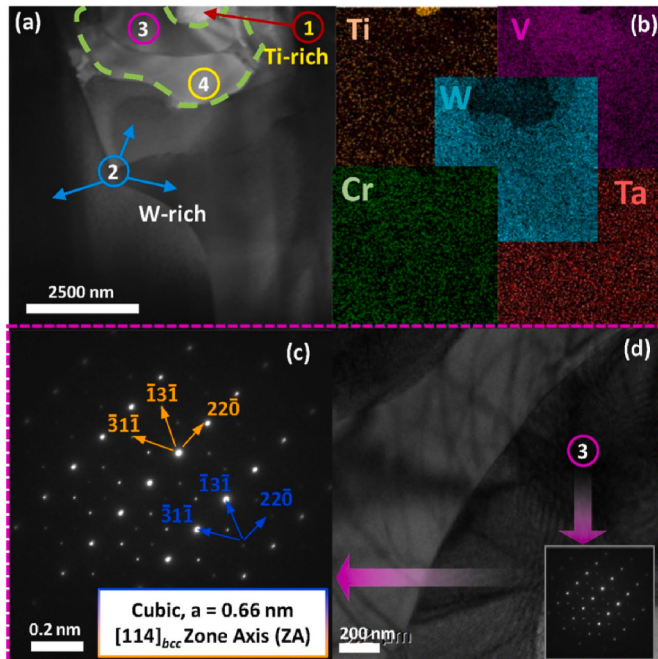


**Fig. 35.** TEM microstructure (a), elemental mapping (b), SADP (c and d) of the C15 laves phase. Reproduced with permission [91].

WMoTaNbC RHEA exhibited fewer and shorter cracks (Fig. 24b). Moreover, pores were also shallower and fewer. The as-deposited WMoTaNbC RHEA had a dense microstructure completely occupied by dendrites, in which, Nb and C atoms were mostly rejected into interdendritic regions. The uniformly distributed Nb and C provided a combined cracking suppression mechanism, Nb as liquid feeding at stage where  $f_s > 0.9$  and formation of Nb-C intermetallics. At last, the

prolonged solidification ranged by the small quantity of eutectic reaction combined with the uniformly distributed liquid by dendrites contributed to lower cracking susceptibility of as-deposited WMoTaNbC RHEA [74].

Xiao et al. investigated WMoTaNbTi RHEAs formed by SEBM with negative defocus distance [75]. At a scanning speed of 4.0 m/s, in-layer cracks, incomplete fused powders and agglomeration of porosity (or totally, named lack of fusion) can be found (Fig. 25a). Decreasing scanning speed led to fewer but larger porosity and smaller incomplete fused areas (Fig. 25b). At scanning speeds of 3.0 m/s and 2.5 m/s, negligible cracks, porosity agglomeration (Fig. 25c) as well as smaller, shallower holes can be found (Fig. 25d) [75].

Popov et al. has reported the production of Al<sub>0.5</sub>CrMoNbTa<sub>0.5</sub> multi-principle alloy using powder bed beam based additive manufacturing [76]. A large number of pores can be found in as-manufactured sample (Fig. 26a,b). Furthermore, they also demonstrated that even an additional step of heat treatment at 1000 °C and 1300 °C had no significant effect on these pores, as shown in Fig. 26c-f.

To sum up, EBM is basically similar to SLM process except the difference of heat sources [77]. Compared with SLM using mirror reflection and rotation to control laser beam movement, EBM relies on magnetic field generated by magnetic deflection coil to control electron beam to move faster without any inertia, and thereby has a faster processing rate [78]. Moreover, EBM is carried out in a vacuum environment, and has the advantages including high energy utilization, no reflection, and high power density, especially suitable for the preparation of RHEAs and brittle materials. At present, the biggest problem in the preparation of RHEAs by AM is that it can not effectively restrain the formation of cracks, which will seriously deteriorate mechanical properties [74]. Besides, AM also shows some other disadvantages, such as high energy consumption, high cost and product size limitations.

#### 4. Microstructure and property regulation

Refractory high-entropy alloys generally exhibit high strength, low

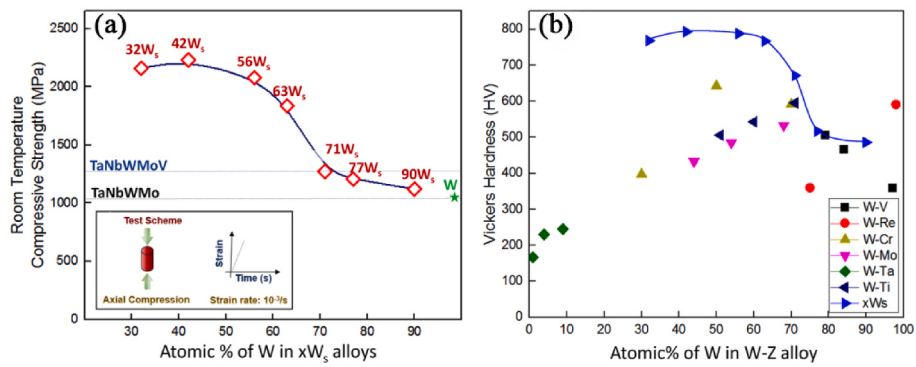


Fig. 36. Compressive properties (a) and Vickers hardness (b) of  $W_xTaTiVCr$  RHEAs and previously reported W-containing RHEAs. Reproduced with permission [91].

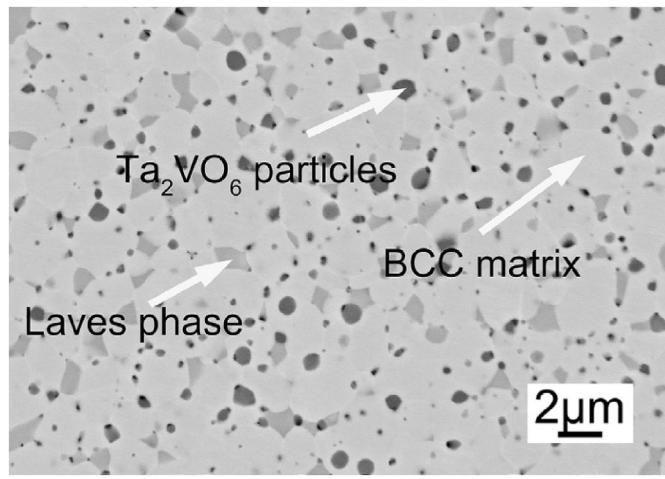


Fig. 37. SEM backscattered electron images of the bulk NbMoTaWVCr HEAs sintered at 1500 °C. Reproduced with permission [32].

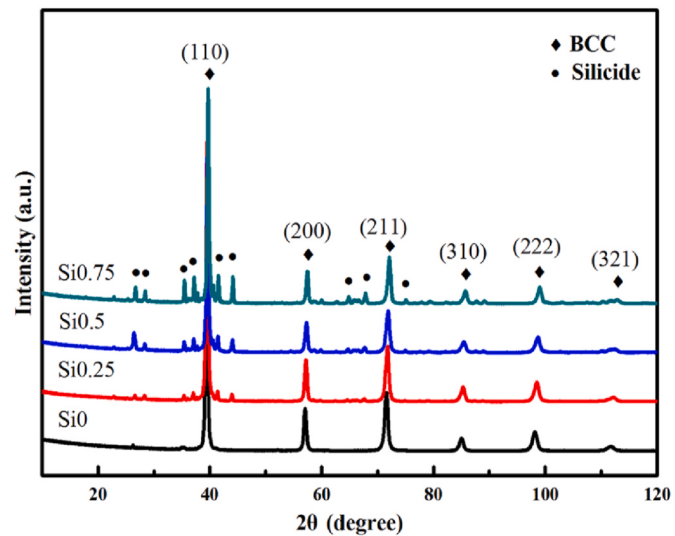


Fig. 39. X-ray diffraction patterns of the as-sintered NbTaWMoSi<sub>x</sub> alloys. Reproduced with permission [93].

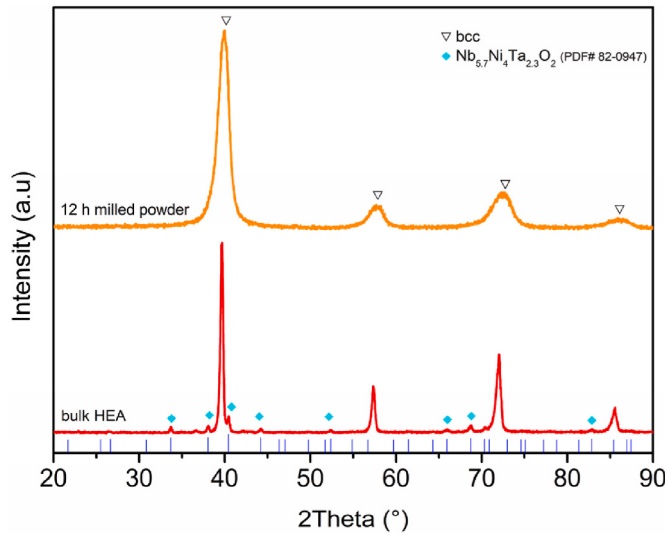


Fig. 38. XRD patterns of RHEA powders after milling for 12 h and bulk specimen sintered at 1700 °C. Reproduced with permission [92].

toughness and brittleness at room temperature, which not only limits their application, but also increases the difficulty of strengthening and toughening. As everyone knows, microstructure is one of the most important factors affecting mechanical properties. Therefore, finding

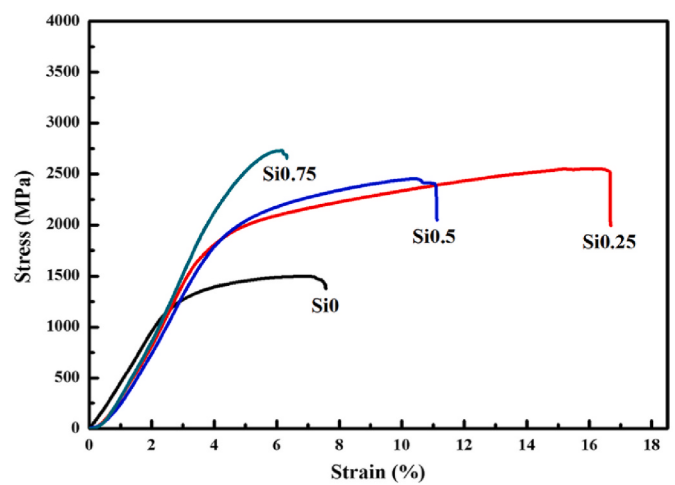
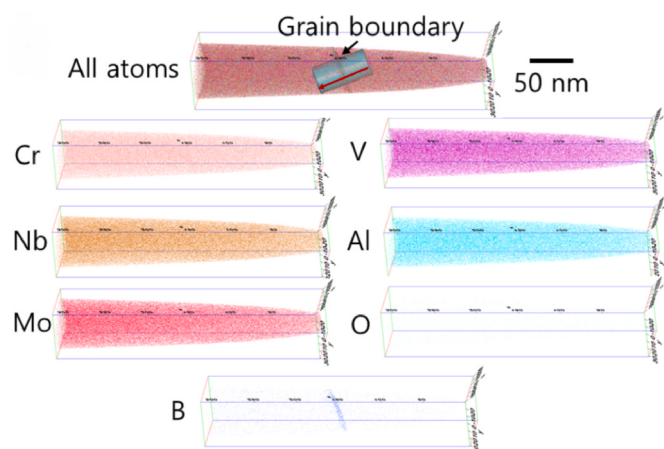
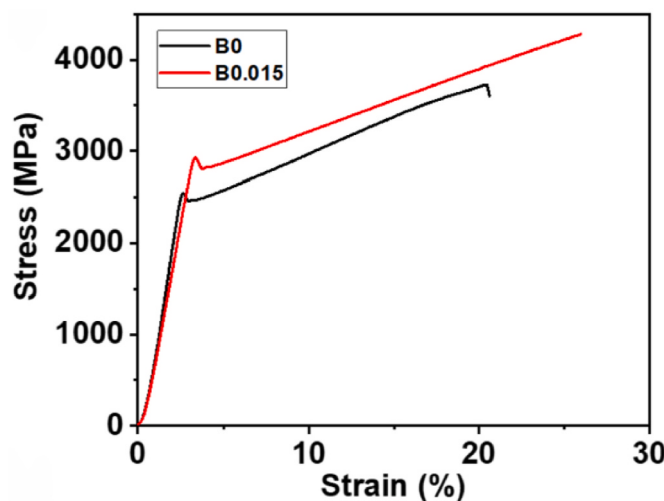


Fig. 40. Compressive stress-strain curves of the SPSed NbTaWMoSi<sub>x</sub> alloys at room temperature. Reproduced with permission [93].

appropriate methods to regulate the microstructure and mechanical properties of RHEAs is the focus and difficulty of current research. This section mainly summarizes the regulation of microstructure and properties in PM RHEAs.



**Fig. 41.** APT reconstructions of the B0.015 alloy across the APT-observed grain boundary along the red arrow. Reproduced with permission [94].



**Fig. 42.** Compressive engineering stress and strain curves of B0 and B0.015 alloys. Reproduced with permission [94].

#### 4.1. Metal elements

In superalloys, adding various elements to form a strengthening phase with high phase stability and high-temperature strength is an effective method for designing high-temperature structural materials [79]. Therefore, for designing RHEAs, metal elements with higher melting points in periodic table will first be selected as the main elements in order to ensure their good high-temperature performance [80]. Table 1 lists the alloying elements that are frequently used in RHEAs.

Cr can combine with refractory metals to form Laves phase with high melting point and medium density. Besides, Cr addition can improve strength, creep resistance, oxidation resistance and hot corrosion resistance at high temperature [81]. The Ti or Zr can effectively reduce the density and improve the specific strength of RHEAs [82]. The addition of Nb can improve ductility of RHEAs, which is the most frequently used element, close to twice as much as Mo [83]. The most direct reason is that Nb has a higher melting point density ratio ( $288\text{ }^{\circ}\text{C g}^{-1}\text{ cm}^{-3}$ ). Thus, the Nb-bearing HEAs show higher melting point and lower density. Ta has good high-temperature softening resistance, high-temperature stability and high elastic modulus [21]. Moreover, in

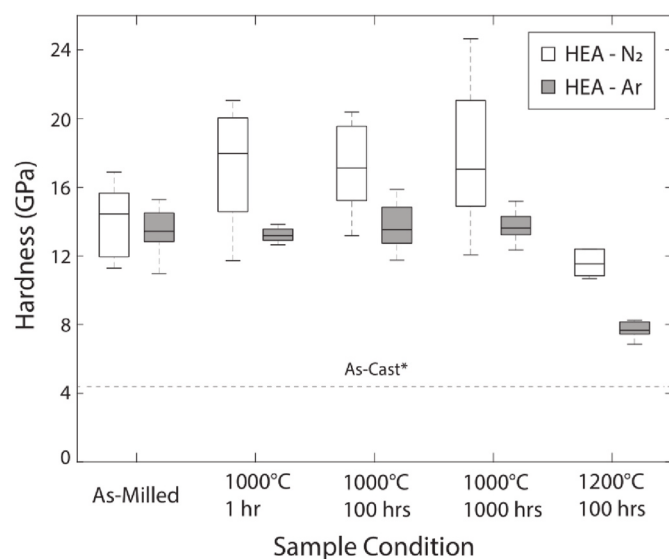


**Fig. 44.** Vicker's microhardness measurements for MoNbTaW RHEAs at each annealing condition. Reproduced with permission [95].

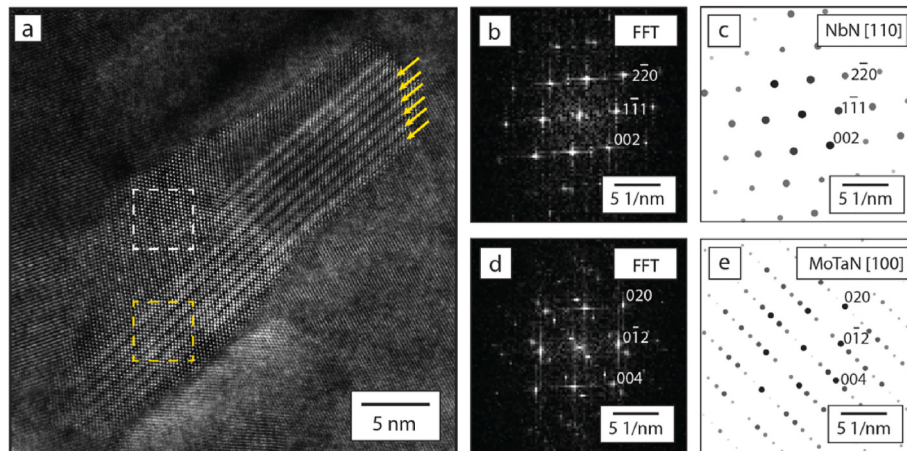


**Fig. 43.** STEM-HAADF image showing orientation relationship between  $(\text{Nb},\text{Ta})_2\text{CN}$  and  $(\text{Mo},\text{W})(\text{Nb},\text{Ta})\text{N}$  (a). Corresponding Fast Fourier Transforms (FFTs) taken from  $(\text{Nb},\text{Ta})_2\text{CN}$  (b) and  $(\text{Mo},\text{W})(\text{Nb},\text{Ta})\text{N}$  (d). The FFTs are consistent with indexed diffraction patterns from the (c) [110] and (e) [100] crystal directions of cubic NbN and tetragonal MoTaN, respectively. Reproduced with permission [95].

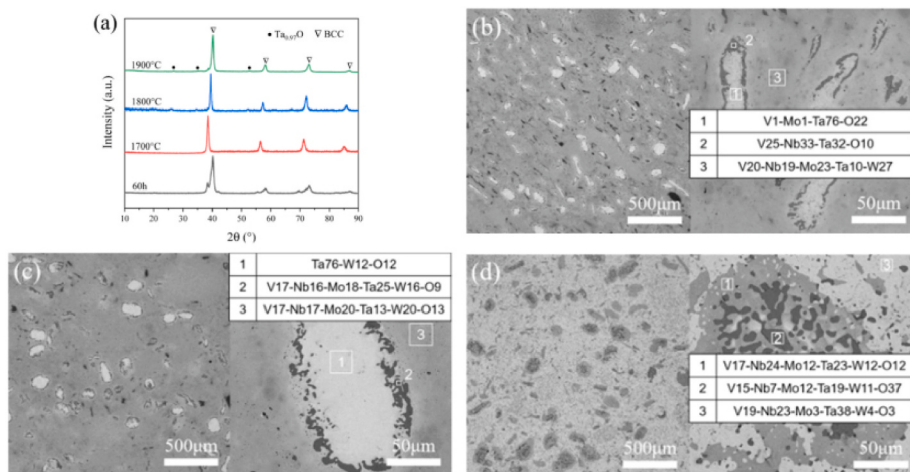


**Fig. 45.** XRD patterns and SEM images of VNbMoTaW alloy sintered at different temperatures for 2 h: (a) XRD, (b) 1700 °C, (c) 1800 °C and (d) 1900 °C. Reproduced with permission [96].

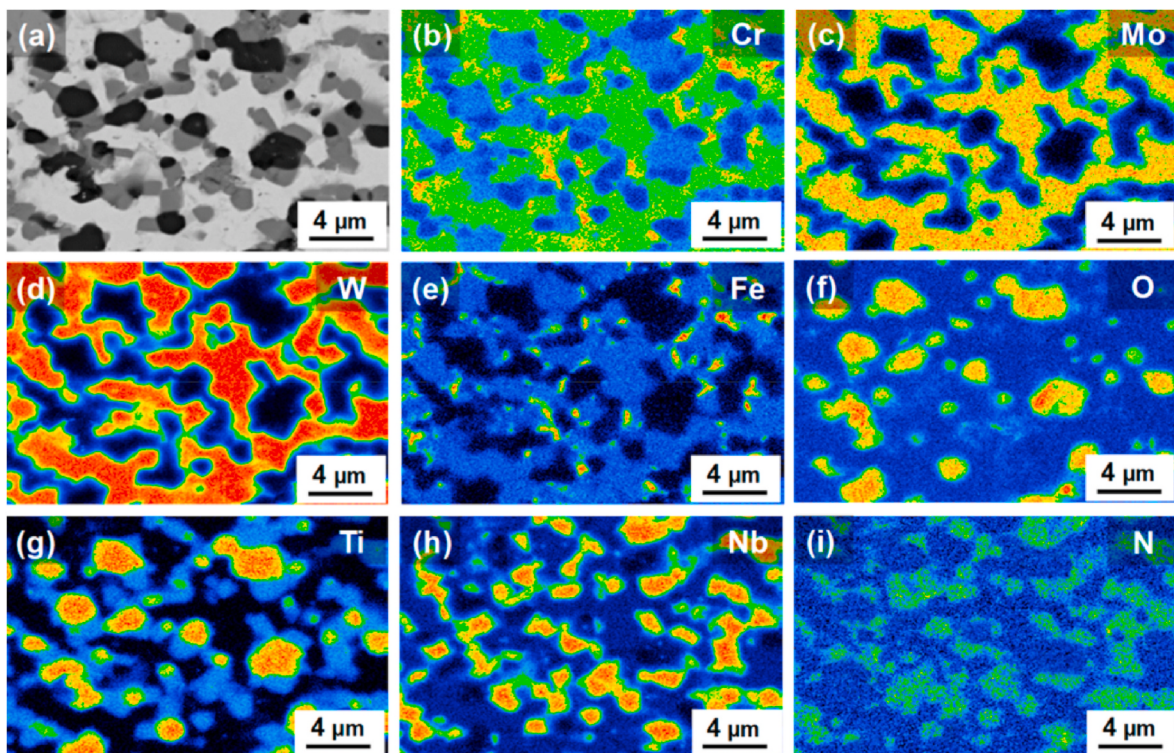


**Fig. 46.** Back-scattered electron (BSE) image (a) and individual elemental mapping (b–i) of the as-sintered CrMoNbWTi–CNO RHEA. Reproduced with permission [97].

order to obtain alloys with excellent properties and clarify the effects of elements on properties [84], studies mainly focused on controlling the type and proportion of elements or adding non-refractory elements, such as O, C, Al and Si.

Ti and Al are introduced in detail as refractory metals and non-refractory metals respectively and are the most frequently used elements to regulating microstructure and properties in existing PM RHEAs.

#### 4.1.1. Titanium (Ti)

Ti exhibits good strength, oxidation resistance and thermal stability at high temperature as well as low valence electron concentration (VEC) and density. Based on these characteristics, Ti is usually selected to

adjust the composition of RHEAs. The Ti addition can effectively resist thermal stress and restrain micro-cracks, so as to improve overall plasticity of material [71].

Ti has been intentionally added to WMoTaNbV RHEA by Long et al. via MA, resulting a significant variation in microstructure and properties [85]. The XRD patterns of WnbMoTaV [38] and WnbMoTaVTi [85] RHEAs are shown in Fig. 27. It is worth noting that the additional BCC2 and FCC phases can form in WnbMoTaVTi RHEA. They speculated that the formation of BCC2 mainly due to inhomogeneous distribution of alloying elements at grain boundaries of sintered RHEA, but it is not possible to determine whether it is resulted from the addition of Ti. Besides, the FCC phase was confirmed to be TiO, which can effectively improve mechanical properties of WMoTaNbVTi RHEA due to the

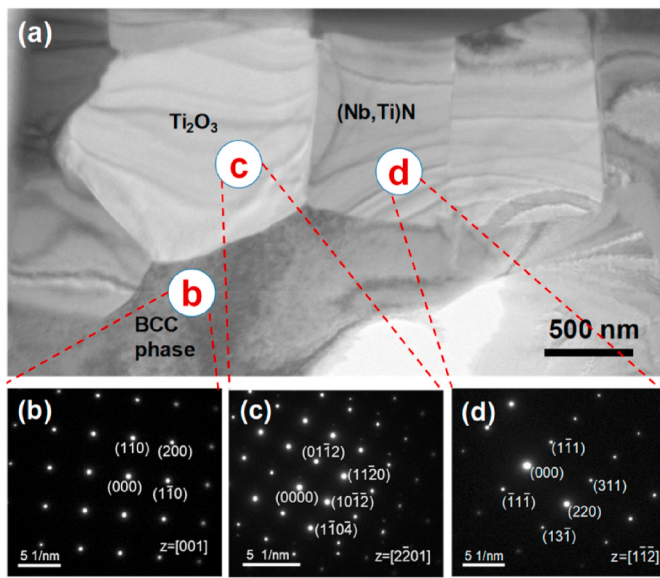


**Fig. 47.** TEM images of CrMoNbWTi–CNO HEA: (a) Bright-field image, diffraction patterns of (b) BCC matrix phase, (c) Ti<sub>2</sub>O<sub>3</sub> phase, (d) (Nb,Ti)N phase. Reproduced with permission [97].

precipitation strengthening [85]. WMoTaNbVTi RHEA exhibited excellent mechanical properties with compressive yield strength of 2709 MPa, fracture strength of 3115 MPa and fracture strain of 11.4% [85].

Pan et al. reported that Ti addition (8 wt%) can further promote the compressive properties in NbMoTaW RHEA, where the fracture strain and peak compressive stress surprisingly increased by 56.5% and 10.7%, respectively (Fig. 28) [86].

Liu et al. investigated the effect of Ti content on microstructure and mechanical properties of Ti<sub>x</sub>VNbMoTa ( $x = 0.5, 1, 1.5, 2$ ) RHEAs systematically [31]. The results showed that higher Ti content resulted in serious aggregation during early stage of MA, leading to the prolongation of MA time (Fig. 29) [31]. Besides, the Ti addition also resulted in the formation of precipitates (compounds of TiN and TiO), as shown in Fig. 30 [31]. The contribution of grain boundary strengthening weakened gradually as the increase of Ti content while the solid solution strengthening and interstitial solid solution strengthening enhanced (Fig. 31) [31]. As Ti content increased, the grain sizes of matrix and precipitates as well as the volume fraction of precipitates increased. The rapid increase in size and volume fraction of precipitates in high Ti-containing (1.5–2 wt%) TiVNbMoTa RHEAs will destroy the coordination of deformation and the continuity of matrix, so as to deteriorate ductility (Fig. 31) [31].

#### 4.1.2. Aluminium (Al)

Although Al shows an FCC crystal structure, it can interact with refractory metals to exchange electrons to form a BCC crystal structure [87]. The atomic radius of Al is similar to that of refractory elements, which means a lower atomic size difference. This has been proven to be one of advantages of forming disordered solid solutions and avoiding intermetallic compounds [84]. The high electron density and high Fermi level of Al tend to promote electron transfer with metals such as V, Nb, Mo, Ta, and W [87]. Al is a p metal with low VEC, and its SP hybrid orbital has strong directionalities. On the other hand, refractory elements are d metals with higher VEC. Thus, adding Al can reduce the VEC effect of system and form strong directional p-d polar bonds, which can promote ordering and reduce bond lengths [84]. The valences of metal atoms are similar (V, Nb and Ta: 6, W and Mo: 5), and the metal bonds between Al atoms are significantly shorter than the sum of corresponding metal radii. When the d shell of refractory metal is almost filled, the addition of Al produces hybridization of the pd shell, forming

a BCC structure [87].

Kang et al. has investigated the effect of Al content on CrNbVMo HREAs in detail [88]. Firstly, phase diagrams of Al<sub>x</sub>CrNbVMo ( $x = 0, 0.5, 1$ ) RHEAs were calculated, indicating that the Al addition can result in the formation of brittle intermetallic phases, such as A15 and Laves (Fig. 32) [88]. Besides, the precipitation of Al<sub>2</sub>O<sub>3</sub> was found as well (Fig. 33) [88], which can lead to Orowan strengthening due to the incoherence of BCC matrices and relatively large size of inclusions [89, 90]. The contributions of each strengthening mechanism to yield strength of Al<sub>0</sub>, Al<sub>0.5</sub>, and Al<sub>1.0</sub> RHEAs are summarized in Fig. 34a. The strengthening contributions resulted from grain boundary strengthening and dislocation strengthening decreased gradually as the increase of Al content [88]. Therefore, although Al<sub>2</sub>O<sub>3</sub> particles can make some contribution to strength due to Orowan strengthening, the addition of Al still resulted in a significant decrease in strength owing to the lack of dislocation strengthening and grain boundary strengthening (Fig. 34b) [88].

Chang et al. studied the influence of Al on powder phase structure and morphology during the MA process of NbVMoTa [42]. A strong polar bond with other elements can form due to the Al addition, which promoted the orderly arrangement of the system. The mixing enthalpy is negative, which can speed up the alloying progress of the system. The fully alloying of (NbVMoTa)<sub>88</sub>Al<sub>12</sub> powder can be achieved at a milling speed of 400 r/min for 60 h, forming a fine-grained RHEA powder with a single BCC structure and a powder particle size of 40~60 nm.

#### 4.1.3. Other metal elements

The W<sub>x</sub>TaTiVCr ( $x = 32, 42, 56, 63, 71, 77, 92$  at.%) RHEAs were manufactured by Waseem et al. via the mixing of elemental W, Ta, Ti, V and Cr powders followed by SPS at 1600 °C [91]. The relative density of these alloys was found to increase with a decrease in the W content. Moreover, C15 Laves phases can form as W content exceeded 70 at.% (Fig. 35) [91]. The increasing lattice strain and solid-solution strengthening produced xWs (when  $x = 32$  to 63 at.%) with hardness and strength levels which were twofold higher than those of pure W and previously reported W-containing RHEAs (Fig. 36) [91].

Long et al. added Cr to NbMoTaWV RHEA by MA to prepare NbMoTaWVCr RHEA [32]. Although only a supersaturated BCC structured solid solution was formed during the MA process, the precipitation of C15 Laves phase ((Cr, V)<sub>2</sub>(Ta, Nb)) was found after sintering at the temperature below 1500 °C (Fig. 37) [32], which was not reported in Cr-free PM NbMoTaWV RHEA [39]. The NbMoTaWVCr alloy sintered at 1500 °C showed an excellent combination of yield strength (3416 MPa) and failure plasticity (5.3%) at room temperature.

A non-equiautomic (W<sub>35</sub>Ta<sub>35</sub>Mo<sub>15</sub>Nb<sub>15</sub>)<sub>95</sub>Ni<sub>5</sub> RHEA was fabricated by Duan et al. via MA and SPS [92]. Minor oxide inclusion (Nb<sub>5.7</sub>Ni<sub>4</sub>Ta<sub>2.3</sub>O<sub>2</sub>) were detected in the bulk sample after sintering at 1700 °C (Fig. 38) [92]. The compressive yield stress, maximum stress and fracture strain of (W<sub>35</sub>Ta<sub>35</sub>Mo<sub>15</sub>Nb<sub>15</sub>)<sub>95</sub>Ni<sub>5</sub> RHEA are 2128 MPa, 2562 MPa and 8.16% respectively, which are superior to some typical RHEAs due to the grain boundary and precipitation strengthening mechanisms.

#### 4.2. Non-metallic elements

The NbTaWMoS<sub>x</sub> ( $x = 0, 0.25, 0.5, 0.75$  wt%) RHEA was successfully prepared by Guo et al. from mixed metal powders using SPS [93]. The Si-free NbTaWMo alloy comprised only one BCC phase, while the addition of Si resulted in the formation of the silicide phase ((Nb, Ta)<sub>5</sub>Si<sub>3</sub>), and its volume fraction increased as the increase in Si content (Fig. 39) [93]. Besides, as the Si content increased, the strength improved while the plasticity decreased due to brittle fracture (Fig. 40) [93]. The yield strength of NbTaWMoS<sub>0.25</sub> alloy was as high as 926 MPa at 1200 °C [93].

The effect of boron (B, 0.015 at.%) on the microstructure and mechanical properties of a PM Al<sub>0.1</sub>CrNbVMo RHEA was investigated by Kang et al. [94]. The doped B atoms segregated along grain boundaries

**Table 2**

Processing, density, microstructure and mechanical properties of recent published PM RHEAs.

Alloys	Processing	Density/g cm <sup>-3</sup>	Phases	Yield strength/MPa	Peak strength/MPa	Refs.
Ti <sub>0.5</sub> VNbMoTa	MA + SPS	9.99	BCC	2563	2723	[31]
Ti <sub>1</sub> VNbMoTa	MA + SPS	9.45	BCC	2208	3238	[31]
Ti <sub>1.5</sub> VNbMoTa	MA + SPS	9.08	BCC + FCC	2696	3034	[31]
Ti <sub>2</sub> VNbMoTa	MA + SPS	8.75	BCC + FCC	2824	3137	[31]
NbMoTaWVCr	MA + SPS	11.06	BCC + Laves + Oxide	3410	3685	[32]
NbMoTaWVCr	MA + SPS	11.16	BCC + Laves + Oxide	3416	3834	[32]
WNbMoTaV	MA + SPS	—	BCC + Ta <sub>2</sub> VO <sub>6</sub>	2612	3472	[38]
NbTaTiV	MA + SPS	—	BCC	1373	2189	[66]
MoNbTaTiV	MA + SPS	9.45	BCC	2208	3238	[83]
NbMoTaWVTi	MA + SPS	10.6	BCC + TiO	2709	3115	[85]
NbMoTaW	MA + SPS	—	BCC	2460	3016	[86]
Ti <sub>8</sub> NbMoTaW	MA + SPS	—	BCC	2377	3340	[86]
CrNbVMo	MA + SPS	8.03	BCC + NbO <sub>0.7</sub>	2743	3200	[88]
Al <sub>0.5</sub> CrNbVMo	MA + SPS	7.53	BCC + Al <sub>2</sub> O <sub>3</sub>	2497	3150	[88]
Al <sub>1</sub> CrNbVMo	MA + SPS	7.05	BCC + Al <sub>2</sub> O <sub>3</sub>	2326	3100	[88]
(W <sub>35</sub> Ta <sub>35</sub> Mo <sub>15</sub> Nb <sub>15</sub> ) <sub>95</sub> Ni <sub>5</sub>	MA + SPS	14.55	BCC + Nb <sub>5.7</sub> Ni <sub>4</sub> Ta <sub>2.3</sub> O <sub>2</sub>	2128	2562	[92]
NbTaWMo	MA + SPS	13.44	BCC + Silicide	1217	1499	[93]
NbTaWMoSi <sub>0.25</sub>	MA + SPS	12.92	BCC + Silicide	1826	2548	[93]
NbTaWMoSi <sub>0.5</sub>	MA + SPS	12.65	BCC + Silicide	1883	2454	[93]
NbTaWMoSi <sub>0.75</sub>	MA + SPS	12.23	BCC + Silicide	2483	2732	[93]
Al <sub>0.1</sub> CrMoNbV	MA + SPS	7.97	BCC + Al <sub>2</sub> O <sub>3</sub>	2544	3726	[94]
Al <sub>0.1</sub> CrMoNbVB <sub>0.015</sub>	MA + SPS	7.97	BCC + Al <sub>2</sub> O <sub>3</sub>	2933	4281	[94]
CrMoNbWTi	MA + SPS	9.85	BCC+(Nb,Ti)N + Ti <sub>2</sub> O <sub>3</sub>	—	4345	[97]
TaTiNb	MA + SPS	—	BCC + FeNb + FeO	1886	2120	[98]
TaTiNbZr	MA + SPS	—	BCC + Zr <sub>2</sub> O	1920	2070	[98]
TaTiNbZrMo	MA + SPS	—	BCC + Zr <sub>2</sub> O	—	1985	[98]
TaTiNbZrW	MA + SPS	—	BCC + Zr <sub>2</sub> O	2458	2665	[98]
VNbMoTaW	MA + Sintering	12.4	BCC + Metal carbide	—	—	[39]
VNbMoTaW	MA + HIP	12.05	BCC + Ta <sub>0.97</sub> O	—	2800	[96]
HfNbTaTiZr	GA + SPS	—	BCC	—	—	[49]
WMoTaNb	SHS + SPS	11.36	SPS + NbO + MgTa <sub>2</sub> O <sub>6</sub> +WO <sub>3</sub>	2080	2910	[62]
TiNbTa <sub>0.5</sub> Zr	Sintering	7.6	BCC	1310	2050	[63]
TiNbTa <sub>0.5</sub> ZrAl <sub>0.2</sub>	Sintering	—	BCC	1500	2000	[63]
TiNbTa <sub>0.5</sub> ZrAl <sub>0.5</sub>	Sintering	7.3	BCC	1740	2031	[64]
W <sub>0.3</sub> (TaTiCrV) <sub>0.7</sub>	SPS	13.4	BCC	2265	2350	[91]
W <sub>0.4</sub> (TaTiCrV) <sub>0.6</sub>	SPS	13.6	BCC	2314	2450	[91]
W <sub>0.5</sub> (TaTiCrV) <sub>0.5</sub>	SPS	14.5	BCC	2144	2200	[91]
W <sub>0.6</sub> (TaTiCrV) <sub>0.4</sub>	SPS	14.9	BCC	2187	2400	[91]
W <sub>0.7</sub> (TaTiCrV) <sub>0.3</sub>	SPS	15.7	BCC	1473	2100	[91]
W <sub>0.8</sub> (TaTiCrV) <sub>0.2</sub>	SPS	16.5	BCC	1208	2000	[91]
W <sub>0.9</sub> (TaTiCrV) <sub>0.1</sub>	SPS	16.5	BCC	1206	1900	[91]
V <sub>0.5</sub> Nb <sub>0.5</sub> ZrTi	SLM	6.5	BCC	1450	2250	[70]
NbMoTa	SLM	—	BCC	1253	1283	[71]
NbMoTaTi	SLM	—	BCC	1201	1380	[71]
NbMoTaNi	SLM	—	BCC	1350	1356	[71]
NbMoTaTi <sub>0.5</sub> Ni <sub>0.5</sub>	SLM	—	BCC	1750	2278	[71]
VNbMoTaW	SLM	—	BCC	—	2154	[73]
WMoTaNbC <sub>5.43</sub>	SEBM	—	BCC + Nb <sub>2</sub> C	—	1221	[74]
WMoTaNbTi	SEBM	—	BCC	1047	1312	[75]

but did not form any boride phases, which was characterized by atom-probe tomography (Fig. 41) [94]. Moreover, adding B can transform fracture surface from intergranular to transgranular due to the enhancing grain boundary cohesion by B segregation, so as to result in improved ductility. The improved yield strength originated from B doping was believed to be attributed to combined effects of dislocation, Orowan and interstitial strengthening. Consequently, the B-doped RHEA showed more superior yield strength of 2933 MPa (15% improvement) and ductility of 25.9% (26% improvement) compared to the undoped RHEA, as shown in Fig. 42 [94].

MoNbTaW RHEA was synthesized by Smeltzer et al. via cryogenic MA and doped with nitrogen by using liquid nitrogen as cryogen [95]. Atomic-resolution characterization determined that this alloy containing coherent (Nb,Ta)<sub>2</sub>CN and (Mo,W)(Nb,Ta)N ceramic phases can deform via a cleavage plane mechanism, as compared to dislocation-based deformation (Fig. 43) [95]. Furthermore, a peak median hardness of 17.8 GPa, an almost 450% improvement compared to its cast relative, was achieved due to the formation of complex nitride phases (Fig. 44) [95].

To reveal the state and influence of oxygen on PM RHEAs, a

VNbMoTaW RHEA was prepared by He et al. via MA and vacuum hot pressing sintering (HPS) [96]. Due to the lowest Gibbs free energy and smallest electronegativity at 1700 °C, a Ta-rich oxide with a grain size about 15 nm formed after sintering. As the sintering temperature increased to 1900 °C, the size of oxide decreased to about 8 nm and dispersed in matrix due to the increase in O solubility and mutual diffusion (Fig. 45) [96]. The ultimate strength of VNbMoTaW RHEA sintered at 1900 °C was as high as 2800 MPa due to Orowan mechanism originated from fine and dispersed oxides [96].

A multiple nonmetallic atoms (C, N, O) co-doped CrMoNbWTi RHEA was prepared by Lv et al. via adding stearic acid and absolute ethanol during milling [97]. Both O and C were completely reacted with refractory metallic elements to in-situ generate massive dispersed refractory compounds of (Nb,Ti)N and Ti<sub>2</sub>O<sub>3</sub>, while C was mainly dissolved in BCC phase (Figs. 46–47) [97]. The as-sintered RHEA exhibited the ultra-high strength and hardness of 4345 MPa and 11.88 GPa respectively, which were not only attributed to the traditional solid solution, grain boundary, second-phase strengthening mechanisms, but also to the additional C interstitial strengthening and dispersed refractory compounds of (Nb,Ti)N and Ti<sub>2</sub>O<sub>3</sub> [97].

The processing, density, microstructure and mechanical properties of recent published powder metallurgy refractory high entropy alloys are collected in Table 2 in order to provide valuable information and references for researchers.

## 5. Summary and outlook

As a widely used advanced structure material in high-temperature fields, refractory high entropy alloys have attracted much attention due to excellent high-temperature strength and phase stability. This paper has systematically reviewed the progress of refractory high-entropy alloys fabricated by powder metallurgy, including the preparation techniques of pre-alloyed powder, powder densification and microstructure and property regulation. Although some progress has been made in recent years, many challenges to further improving the properties of powder metallurgy refractory high-entropy alloys and expanding their application fields are still faced, as follows.

- (1) Mechanical alloying is currently the most commonly used and favored method for preparing refractory high-entropy alloy powders. Although nanoscale pre-alloyed powder with uniform alloy composition can be obtained, it has a fatal shortcoming, that is, the milling process will inevitably produce C, N and O contamination even under argon protective atmosphere. The focus of subsequent studies may need to be devoted to completely avoiding or mitigating C, N and O contamination, thereby further improving the properties of refractory high-entropy alloys fabricated by powder metallurgy.
- (2) Powder metallurgy has significant advantages in the preparation of refractory high-entropy alloys. The prepared materials have advantages of uniform composition, fine structure and dispersed distribution of second phases, showing better microstructure and mechanical properties than melted alloys. However, the composition design of powder metallurgy refractory high-entropy alloys needs to consider factors such as mutual solubility, mixing enthalpy and melting point differences between components to avoid problems such as the formation of terminal solid solutions, intermetallic compounds or precipitates during preparation process.
- (3) The high-temperature structural stability, high-temperature mechanical behavior, fatigue damage behavior under cyclic loading and functional properties such as energy storage, magnetism and catalysis of powder metallurgy refractory high-entropy alloys also need further study. Moreover, preparing refractory high-entropy alloys with special dislocation structures, microstructure and properties through additive manufacturing may become a promising research direction on basic theory and engineering applications of powder metallurgy refractory high-entropy alloys in the future.
- (4) Although a large number of composition systems have been developed in the field of powder metallurgy refractory high-entropy alloys, but the physical metallurgical foundations are still immature. It is also necessary to conduct in-depth and systematic research on the solid solution effect, clarify the synergistic effects of different elements and create microstructure and excellent properties that are difficult to obtain in conventional preparation method by developing reliable experimental and computational thermodynamics databases.

## Declaration of competing interest

The authors declare that they have no known competing financial interests or personal relationships that could have appeared to influence the work reported in this paper.

## Acknowledgements

The authors gratefully acknowledge the financial support received from the Key Research and Development Program of Shaanxi Province (Grant No. 2024GX-YBXM-367), Postdoctoral Research Project Funding of Shaanxi Province (Grant No. 2023BSHGZZHQYXMZZ23).

## References

- [1] J.W. Yeh, S.K. Chen, S.J. Lin, J.Y. Gan, T.S. Chin, T.T. Shun, C.H. Tsau, S.Y. Chang, Nanostructured high-entropy alloys with multiple principal elements: novel alloy design concepts and outcomes, *Adv. Eng. Mater.* 6 (5) (2004) 299–303.
- [2] K.Y. Tsai, M.H. Tsai, J.W. Yeh, Sluggish diffusion in Co–Cr–Fe–Mn–Ni high-entropy alloys, *Acta Mater.* 61 (13) (2013) 4887–4897.
- [3] Y. Jien-Wei, Recent progress in high entropy alloys, *Ann. Chim. Sci. Mat.* 31 (6) (2006) 633–648.
- [4] S. Ranganathan, Aligned pleasures: multimetalllic cocktails, *Curr. Sci. India* 85 (5) (2003) 1404–1406.
- [5] W. Xiong, A.X.Y. Guo, S. Zhan, C.-T. Liu, S.C. Cao, Refractory high-entropy alloys: a focused review of preparation methods and properties, *J. Mater. Sci. Technol.* 142 (2023) 196–215.
- [6] O.N. Senkov, D.B. Miracle, K.J. Chaput, J.-P. Couzinie, Development and exploration of refractory high entropy alloys—a review, *J. Mater. Res.* 33 (19) (2018) 3092–3128.
- [7] W. Zheng, S. Lü, S. Wu, X. Chen, W. Guo, Development of MoNbVTax refractory high entropy alloy with high strength at elevated temperature, *Mater. Sci. Eng., A* 850 (2022) 143554.
- [8] O.N. Senkov, G.B. Wilks, J.M. Scott, D.B. Miracle, Mechanical properties of Nb<sub>25</sub>Mo<sub>25</sub>Ta<sub>25</sub>W<sub>25</sub> and V<sub>20</sub>Nb<sub>20</sub>Mo<sub>20</sub>Ta<sub>20</sub>W<sub>20</sub> refractory high entropy alloys, *Intermetallics* 19 (5) (2011) 698–706.
- [9] X. Ren, Y. Li, Y. Qi, B. Wang, Review on preparation technology and properties of refractory high entropy alloys, *Materials* 15 (8) (2022) 2931.
- [10] Y.H. Meng, F.H. Duan, J. Pan, Y. Li, Phase stability of B2-ordered ZrTiHfCuNiFe high entropy alloy, *Intermetallics* 111 (2019) 106515.
- [11] K. Ren, H. Liu, R. Chen, Y. Tang, B. Guo, S. Li, J. Wang, R. Wang, F. Lu, Compression properties and impact energy release characteristics of TiZrNbV high-entropy alloy, *Mater. Sci. Eng., A* 827 (2021) 142074.
- [12] L. Tao, M. Sun, Y. Zhou, M. Luo, F. Lv, M. Li, Q. Zhang, L. Gu, B. Huang, S. Guo, A general synthetic method for high-entropy alloy subnanometer ribbons, *J. Am. Chem. Soc.* 144 (23) (2022) 10582–10590.
- [13] S.-J. Wei, H.-X. Shen, L.-Y. Zhang, L. Luo, X.-X. Tang, J.-F. Sun, X.-Q. Li, Microstructure and magnetocaloric properties of melt-extracted SmGdDyCoAl high-entropy amorphous microwires, *Rare Met.* (2023) 1–9.
- [14] W. Sheng, J.Q. Wang, G. Wang, J. Huo, X. Wang, R.W. Li, Amorphous microwires of high entropy alloys with large magnetocaloric effect, *Intermetallics* 96 (2018) 79–83.
- [15] L. Luo, H. Shen, Y. Bao, H. Yin, S.J. A, Y. Huang, S. Guo, S. Gao, D. Xing, Z. Li, Magnetocaloric effect of melt-extracted high-entropy Gd<sub>19</sub>Tb<sub>1</sub>Er<sub>18</sub>Fe<sub>19</sub>Al<sub>25</sub> amorphous microwires, *J. Magn. Magn. Mater.* 507 (2020) 166856.
- [16] O.N. Senkov, G.B. Wilks, D.B. Miracle, C.P. Chuang, P.K. Liaw, Refractory high-entropy alloys, *Intermetallics* 18 (9) (2010) 1758–1765.
- [17] Z. Zhang, H. Zhang, Y. Tang, Y. Ye, S. Li, S. Bai, Microstructure, mechanical properties and energetic characteristics of a novel high-entropy alloy HfZrTiTa<sub>0.53</sub>, *Mater. Des.* 133 (2017) 435–443.
- [18] N.D. Stepanov, N.Y. Yurchenko, S.V. Zherebtsov, M.A. Tikhonovsky, G. A. Salishchev, Aging behavior of the HfNbTaTiZr high entropy alloy, *Mater. Lett.* 211 (15) (2018) 87–90.
- [19] J. Iek, P. Haulid, M. Cieslar, O. Melikhova, H.S. Kim, Strength enhancement of high entropy alloy HfNbTaTiZr by severe plastic deformation, *J. Alloys Compd.* 768 (2018) 924–937.
- [20] L. Zhang, X. Li, X. Qu, M. Qin, Z. Que, Z. Wei, C. Guo, X. Lu, Y. Dong, Powder metallurgy route to ultrafine-grained refractory metals, *Adv. Mater.* (2022) 2205807.
- [21] C. Zhu, Z. Li, C. Hong, P. Dai, J. Chen, Microstructure and mechanical properties of the TiZrNbMoTa refractory high-entropy alloy produced by mechanical alloying and spark plasma sintering, *Int. J. Refract. Met. Hard Mater.* 93 (2020) 105357.
- [22] P. Novak, Advanced powder metallurgy technologies, *Materials* 13 (7) (2020) 1742.
- [23] Y. Chen, R. Yang, C. Zhang, J. Song, Y. Che, J. He, Novel process for preparing tungsten powder by hydrogen reduction of tungsten trioxide, *Int. J. Refract. Met. Hard Mater.* 106 (2022) 105869.
- [24] K.A. Abdullin, A. Azatkaliev, M.T. Gabdullin, Z.K. Kalkozova, B.N. Mukashev, A. S. Serikhanov, Preparation of nanosized tungsten and tungsten oxide powders, *Phys. Solid State* 61 (1) (2019) 163–168.
- [25] H. Zhang, Z.-B. Li, G.-H. Zhang, K.-C. Chou, A novel method for preparing ultrafine molybdenum powder, *Int. J. Refract. Met. Hard Mater.* 96 (2021) 105491.
- [26] G. Mai, C. Zhang, J. Song, Y. Che, J. He, Preparation of highly uniform molybdenum powder by the short-process reduction of molybdenum trioxide with hydrogen, *Int. J. Refract. Met. Hard Mater.* 100 (2021) 105644.
- [27] Q. Li, B. Zhang, Y. Wen, G. Chen, Y. Wang, P. Wang, X. Qu, A comprehensive study of tantalum powder preparation for additive manufacturing, *Appl. Surf. Sci.* 593 (2022) 153357.

- [28] V. Orlov, T.Y. Prokhorova, Heat treatment of tantalum and niobium powders prepared by magnesium-thermic reduction, *Russ. Metall.* 2017 (2017) 905–911.
- [29] Y. Xia, J. Zhao, Z. Dong, X. Guo, Q. Tian, S. Zhang, Y. Liu, Two-step gradient reduction of zirconia for making high-purity zirconium powder, *JOM* 72 (2020) 1687–1693.
- [30] T. Gu, L.-M. Wang, Q. Hu, X.-B. Liang, D.-X. Fu, Y.-X. Chen, X.-M. Zhao, Y.-W. Sheng, Effect of mechanical alloying and sintering behavior on the microstructure and properties of NbMoTaWRe refractory high entropy alloy, *Met. Mater. Int.* 28 (11) (2022) 2571–2582.
- [31] Q. Liu, G. Wang, X. Sui, Y. Xu, Y. Liu, J. Yang, Ultra-fine grain Ti<sub>x</sub>VNbMoTa refractory high-entropy alloys with superior mechanical properties fabricated by powder metallurgy, *J. Alloys Compd.* 865 (2021) 158592.
- [32] Y. Long, X. Liang, K. Su, H. Peng, X. Li, A fine-grained NbMoTaWCr refractory high-entropy alloy with ultra-high strength: microstructural evolution and mechanical properties, *J. Alloys Compd.* 780 (2019) 607–617.
- [33] B.-r. Ke, Y.-c. Sun, Y. Zhang, W.-r. Wang, W.-m. Wang, P.-y. Ma, W. Ji, Z.-y. Fu, Powder metallurgy of high-entropy alloys and related composites: a short review, *Int. J. Miner. Metall. Mater.* 28 (6) (2021) 931–943.
- [34] C. Suryanarayana, Mechanical alloying and milling, *Prog. Mater. Sci.* 46 (1–2) (2001) 1–184.
- [35] A. Roh, D. Kim, S. Nam, D.-I. Kim, H.-Y. Kim, K.-A. Lee, H. Choi, J.-H. Kim, NbMoTaW refractory high entropy alloy composites strengthened by in-situ metal-non-metal compounds, *J. Alloys Compd.* 822 (2020) 153423.
- [36] S. Das, P.S. Robi, A novel refractory WMoCrTa high-entropy alloy possessing fine combination of compressive stress-strain and high hardness properties, *Adv. Powder Technol.* 31 (12) (2020) 4619–4631.
- [37] N. Shkodich, M. Spasova, M. Farle, D.Y. Kovalev, A. Nepapushev, K. Kuskov, Y. S. Vergunova, Y.B. Scheck, A. Rogachev, Structural evolution and magnetic properties of high-entropy CuCrFeTiNi alloys prepared by high-energy ball milling and spark plasma sintering, *J. Alloys Compd.* 816 (2020) 152611.
- [38] B. Kang, J. Lee, H.J. Ryu, S.H. Hong, Ultra-high strength WNbMoTaV high-entropy alloys with fine grain structure fabricated by powder metallurgical process, *Mater. Sci. Eng., A* 712 (2018) 616–624.
- [39] S. Xin, M. Zhang, T. Yang, Y. Zhao, B. Sun, T. Shen, Ultrahard bulk nanocrystalline VNbMoTaW high-entropy alloy, *J. Alloys Compd.* 769 (2018) 597–604.
- [40] G. Wang, Q. Liu, J. Yang, X. Li, X. Sui, Y. Gu, Y. Liu, Synthesis and thermal stability of a nanocrystalline MoNbTaTiV refractory high-entropy alloy via mechanical alloying, *Int. J. Refract. Met. Hard Mater.* 84 (2019) 104988.
- [41] G. Williamson, W. Hall, X-ray line broadening from filed aluminium and wolfram, *Acta Metall.* 1 (1) (1953) 22–31.
- [42] D. Chang, L. Deng, J. Luo, Effects of ball milling process and alloying element Al on preparation of NbVMoTa high entropy alloy powders by mechanical alloying, *Mater. Rep.* 37 (10) (2023) 21110231.
- [43] G. Nan, L. Yan, P. Haiyan, Z. Weihua, P. Liang, Microstructure and mechanical properties of TiVNbTa refractory high-entropy alloy prepared by powder metallurgy, *Chin. J. Mater. Res.* 33 (8) (2019) 572–578.
- [44] M.H. Seizo Nagasaki, A.S. Liu, *Binary Alloy Phase Diagrams*, fourth ed., Metallurgical Industry Press, Beijing, 2004.
- [45] S. Chen, C. Qi, J. Liu, J. Zhang, Y. Wu, Recent advances in W-containing refractory high-entropy alloys—an overview, *Entropy* 24 (11) (2022) 1553.
- [46] S. Gao, A. Fu, Z. Xie, T. Liao, Y. Cao, B. Liu, Preparation and microstructure of high-activity spherical TaNbTiZr refractory high-entropy alloy powders, *Materials* 16 (2) (2023) 791.
- [47] F. Pengjun, X. Yi, L. Xinggang, C. Ya, Influence of atomizing gas and cooling rate on solidification characterization of nickel-based superalloy powders, *Rare Met. Mater. Eng.* 47 (2) (2018) 423–430.
- [48] L. Ramírez-Vidaurri, M. Castro-Román, M. Herrera-Trejo, C. García-López, E. Almanza-Casas, Cooling rate and carbon content effect on the fraction of secondary phases precipitate in as-cast microstructure of ASTM F75 alloy, *J. Mater. Process. Technol.* 209 (4) (2009) 1681–1687.
- [49] F. Lukac, M. Budr, R. Musalek, J. Klecka, J. Cinert, J. Cizek, T. Chraska, J. Cizek, O. Melikhova, J. Kuriplach, J. Zyka, J. Malek, Spark plasma sintering of gas atomized high-entropy alloy HfNbTaTiZr, *J. Mater. Res.* 33 (19) (2018) 3247–3257.
- [50] J. Malek, J. Zyka, F. Lukac, M. Vilemova, T. Vlasak, J. Cizek, O. Melikhova, A. Machackova, H.S. Kim, The effect of processing route on properties of HfNbTaTiZr high entropy alloy, *Materials* 12 (23) (2019) 4022.
- [51] J. Couzinié, G. Dirras, L. Perrière, T. Chauveau, E. Leroy, Y. Champion, I. Guillot, Microstructure of a near-equimolar refractory high-entropy alloy, *Mater. Lett.* 126 (2014) 285–287.
- [52] G. Chen, S.Y. Zhao, P. Tan, J. Wang, C.S. Xiang, H.P. Tang, A comparative study of Ti-6Al-4V powders for additive manufacturing by gas atomization, plasma rotating electrode process and plasma atomization, *Powder Technol.* 333 (2018) 38–46.
- [53] Y. Nie, J. Tang, B. Yang, Q. Lei, S. Yu, Y. Li, Comparison in characteristic and atomization behavior of metallic powders produced by plasma rotating electrode process, *Adv. Powder Technol.* 31 (5) (2020) 2152–2160.
- [54] Q. Li, L. Zhang, X. Chen, D. Wei, P. Zhang, Y. Chen, X. Qu, Characterization of plasma rotating electrode atomized Nb-Ti based alloy powder, *Met. Powder Rep.* 75 (2) (2020) 82–91.
- [55] Y. Liu, S. Liang, Z. Han, J. Song, Q. Wang, A novel model of calculating particle sizes in plasma rotating electrode process for superalloys, *Powder Technol.* 336 (2018) 406–414.
- [56] M. Xia, Y. Chen, K. Chen, Y. Tong, X. Liang, B. Shen, Synthesis of WTaMoNbBz refractory high-entropy alloy powder by plasma spheroidization process for additive manufacturing, *J. Alloys Compd.* 917 (2022) 165501.
- [57] B. Liu, H. Duan, L. Li, C. Zhou, J. He, H. Wu, Microstructure and mechanical properties of ultra-hard spherical refractory high-entropy alloy powders fabricated by plasma spheroidization, *Powder Technol.* 382 (2021) 550–555.
- [58] M. Xia, Y. Chen, R. Wang, X. Liang, B. Shen, Fabrication of spherical MoNbTaWCr refractory high-entropy powders by spray granulation combined with plasma spheroidization, *J. Alloys Compd.* 931 (2023) 167542.
- [59] H. Hedger, A. Hall, Preliminary observations on the use of the induction-coupled plasma torch for the preparation of spherical powder, *Powder Metall.* 4 (8) (1961) 65–72.
- [60] J. Subrahmanyam, M. Vijayakumar, Self-propagating high-temperature synthesis, *J. Mater. Sci.* 27 (1992) 6249–6273.
- [61] S. Dine, V. Kentheshwaran, D. Vrel, J.-P. Couzinié, G. Dirras, Synthesis of nanometric MoNbW alloy using self-propagating high-temperature synthesis, *Adv. Powder Technol.* 28 (7) (2017) 1739–1744.
- [62] M. Moser, S. Dine, D. Vrel, L. Perrière, R. Pires-Brazuna, H. Couque, F. Bernard, Elaboration and characterization of WMoTaNb high entropy alloy prepared by powder metallurgy processes, *Materials* 15 (15) (2022) 5416.
- [63] Y. Cao, Y. Liu, B. Liu, W. Zhang, Precipitation behavior during hot deformation of powder metallurgy Ti-Nb-Ta-Zr-Al high entropy alloys, *Intermetallics* 100 (2018) 95–103.
- [64] Y. Cao, Y. Liu, Y. Li, B. Liu, A. Fu, Y. Nie, Precipitation behavior and mechanical properties of a hot-worked TiNbTa<sub>0.5</sub>ZrAl<sub>0.5</sub> refractory high entropy alloy, *Int. J. Refract. Met. Hard Mater.* 86 (2020) 105132.
- [65] Z.-H. Zhang, Z.-F. Liu, J.-F. Lu, X.-B. Shen, F.-C. Wang, Y.-D. Wang, The sintering mechanism in spark plasma sintering – proof of the occurrence of spark discharge, *Scripta Mater.* 81 (2014) 56–59.
- [66] W. Guo, B. Liu, Y. Liu, T. Li, A. Fu, Q. Fang, Y. Nie, Microstructures and mechanical properties of ductile NbTaTiV refractory high entropy alloy prepared by powder metallurgy, *J. Alloys Compd.* 776 (2019) 428–436.
- [67] G. Dirras, J. Gubicza, A. Heczel, L. Lilienstern, J.P. Couzinié, L. Perrière, I. Guillot, A. Hocini, Microstructural investigation of plastically deformed Ti20Zr20Hf20Nb20Ta20 high entropy alloy by X-ray diffraction and transmission electron microscopy, *Mater. Char.* 108 (2015) 1–7.
- [68] L.E. Murr, E. Martinez, K.N. Amato, S.M. Gaytan, J. Hernandez, D.A. Ramirez, P. W. Shindo, F. Medina, R.B. Wicker, Fabrication of metal and alloy components by additive manufacturing: examples of 3D materials science, *J. Mater. Res. Technol.* 1 (1) (2012) 42–54.
- [69] X. Xie, N. Li, W. Liu, S. Huang, X. He, Q. Yu, H. Xiong, E. Wang, X. Hou, Research progress of refractory high entropy alloys: a review, *Chin. J. Mech. Eng.* 35 (1) (2022) 142–163.
- [70] P. Zhu, Y. Yu, C. Zhang, Q. Zhou, B. An, R. Guo, K.C. Chan, L. Liu, V<sub>0.5</sub>Nb<sub>0.5</sub>ZrTi refractory high-entropy alloy fabricated by laser additive manufacturing using elemental powders, *Int. J. Refract. Met. Hard Mater.* 113 (2023) 106220.
- [71] H. Zhang, Y. Zhao, J. Cai, S. Ji, J. Geng, X. Sun, D. Li, High-strength NbMoTaX refractory high-entropy alloy with low stacking fault energy eutectic phase via laser additive manufacturing, *Mater. Des.* 201 (2021) 109462.
- [72] F. Huber, D. Bartels, M. Schmidt, In-Situ Alloy Formation of a WMoTaNbV Refractory metal high entropy alloy by laser powder bed fusion (PBF-LB/M), *Materials* 14 (11) (2021) 3095.
- [73] P. Gu, T. Qi, L. Chen, T. Ge, X. Ren, Manufacturing and analysis of VNbMoTaW refractory high-entropy alloy fabricated by selective laser melting, *Int. J. Refract. Met. Hard Mater.* 105 (2022) 105834.
- [74] B. Xiao, H. Liu, W. Jia, J. Wang, L. Zhou, Cracking suppression in selective electron beam melted WMoTaNbC refractory high-entropy alloy, *J. Alloys Compd.* 948 (2023) 169787.
- [75] B. Xiao, W. Jia, H. Tang, J. Wang, L. Zhou, Microstructure and mechanical properties of WMoTaNbTi refractory high-entropy alloys fabricated by selective electron beam melting, *J. Mater. Sci. Technol.* 108 (2022) 54–63.
- [76] V.V. Popov, A. Katz-Demyanetz, A. Koptyug, M. Bamberger, Selective electron beam melting of Al<sub>0.5</sub>CrMoNbTa<sub>0.5</sub> high entropy alloys using elemental powder blend, *Heliyon* 5 (2) (2019) e01188.
- [77] X. Xie, N. Li, W. Liu, S. Huang, X. He, Q. Yu, H. Xiong, E. Wang, X. Hou, Research progress of refractory high entropy alloys: a Review, *Chin. J. Mech. Eng.* 35 (1) (2022) 142.
- [78] M. Galati, L. Iuliano, A literature review of powder-based electron beam melting focusing on numerical simulations, *Addit. Manuf.* 19 (2018) 1–20.
- [79] X. Gao, L. Wang, N. Guo, L. Luo, G. Zhu, C. Shi, Y. Su, J. Guo, In-situ development of MB<sub>2</sub> and their effect on microstructure and mechanical properties of refractory Hf<sub>0.5</sub>Mo<sub>0.5</sub>NbTiZr high entropy alloy matrix composites, *Int. J. Refract. Met. Hard Mater.* 96 (2021) 105473.
- [80] S. Das, P. Robi, A novel refractory WMoCrTa high-entropy alloy possessing fine combination of compressive stress-strain and high hardness properties, *Adv. Powder Technol.* 31 (12) (2020) 4619–4631.
- [81] X. Gao, L. Wang, N. Guo, L. Luo, G. Zhu, C. Shi, Y. Su, J. Guo, Microstructure characteristics and mechanical properties of Hf<sub>0.5</sub>Mo<sub>0.5</sub>NbTiZr refractory high entropy alloy with Cr addition, *Int. J. Refract. Met. Hard Mater.* 95 (2021) 105405.
- [82] M. Zhu, L. Yao, Y. Liu, M. Zhang, K. Li, Z. Jian, Microstructure evolution and mechanical properties of a novel CrNbTiZrAlx (0.25≤x≤1.25) eutectic refractory high-entropy alloy, *Mater. Lett.* 272 (2020) 127869.
- [83] Q. Liu, G. Wang, X. Sui, Y. Liu, X. Li, J. Yang, Microstructure and mechanical properties of ultra-fine grained MoNbTaTiV refractory high-entropy alloy fabricated by spark plasma sintering, *J. Mater. Sci. Technol.* 35 (11) (2019) 2600–2607.
- [84] S. Ge, H. Fu, L. Zhang, H. Mao, H. Li, A. Wang, W. Li, H. Zhang, Effects of Al addition on the microstructures and properties of MoNbTaTiV refractory high entropy alloy, *Mater. Sci. Eng., A* 784 (2020) 139275.

- [85] Y. Long, K. Su, J. Zhang, X. Liang, H. Peng, X. Li, Enhanced strength of a mechanical alloyed NbMoTaWVTi refractory high entropy alloy, *Materials* 11 (5) (2018) 669.
- [86] J. Pan, T. Dai, T. Lu, X. Ni, J. Dai, M. Li, Microstructure and mechanical properties of Nb<sub>25</sub>Mo<sub>25</sub>Ta<sub>25</sub>W<sub>25</sub> and Ti<sub>8</sub>Nb<sub>23</sub>Mo<sub>23</sub>Ta<sub>23</sub>W<sub>23</sub> high entropy alloys prepared by mechanical alloying and spark plasma sintering, *Mater. Sci. Eng., A* 738 (2018) 362–366.
- [87] X. Liu, Z. Bai, X. Ding, J. Yao, L. Wang, Y. Su, Z. Fan, J. Guo, A novel light-weight refractory high-entropy alloy with high specific strength and intrinsic deformability, *Mater. Lett.* 287 (2021) 129255.
- [88] B. Kang, T. Kong, H.J. Ryu, S.H. Hong, Superior mechanical properties and strengthening mechanisms of lightweight Al<sub>x</sub>CrNbVMo refractory high-entropy alloys ( $x = 0, 0.5, 1.0$ ) fabricated by the powder metallurgy process, *J. Mater. Sci. Technol.* 69 (2020) 32–41.
- [89] P. Wang, H. Cai, S. Zhou, L. Xu, Processing, microstructure and properties of Ni<sub>1.5</sub>CoCuFeCr<sub>0.5</sub>–xVx high entropy alloys with carbon introduced from process control agent, *J. Alloys Compd.* 695 (2017) 462–475.
- [90] A. Argon, Strengthening Mechanisms in Crystal Plasticity, OUP, Oxford, 2007.
- [91] O.A. Waseem, H.J. Ryu, Powder metallurgy processing of a W(x)TaTiVCr high-entropy alloy and its derivative alloys for fusion material applications, *Sci. Rep.* 7 (1) (2017) 1926.
- [92] B. Duan, Y. Yu, X. Liu, D. Wang, Z. Wu, A Novel Non-Equiautomic (W<sub>35</sub>Ta<sub>35</sub>Mo<sub>15</sub>Nb<sub>15</sub>)<sub>95</sub>Ni<sub>5</sub> refractory high entropy alloy with high density fabricated by powder metallurgical process, *Metals* 10 (11) (2020) 1436.
- [93] Z. Guo, A. Zhang, J. Han, J. Meng, Effect of Si additions on microstructure and mechanical properties of refractory NbTaWMo high-entropy alloys, *J. Mater. Sci.* 54 (7) (2019) 5844–5851.
- [94] B. Kang, T. Kong, N.H. Dan, D.D. Phuong, H.J. Ryu, S.H. Hong, Effect of boron addition on the microstructure and mechanical properties of refractory Al<sub>0.1</sub>CrNbVMo high-entropy alloy, *Int. J. Refract. Met. Hard Mater.* 100 (2021) 105636.
- [95] J.A. Smeltzer, B.C. Hornbuckle, A.K. Giri, K.A. Darling, M.P. Harmer, H.M. Chan, C. J. Marvel, Nitrogen-induced hardening of refractory high entropy alloys containing laminar ordered phases, *Acta Mater.* 211 (2021) 116884.
- [96] J. He, Y. Qiao, R. Wang, Y. Tang, S. Li, X. Liu, Y. Ye, L.a. Zhu, Z. Wang, S. Bai, State and effect of oxygen on high entropy alloys prepared by powder metallurgy, *J. Alloys Compd.* 891 (2022) 161963.
- [97] S. Lv, Y. Zu, G. Chen, B. Zhao, X. Fu, W. Zhou, A multiple nonmetallic atoms co-doped CrMoNbWTi refractory high-entropy alloy with ultra-high strength and hardness, *Mater. Sci. Eng., A* 795 (2020) 140035.
- [98] N. Shkodich, K. Kuskov, A. Sedegov, I. Kovalev, A. Pantelieeva, Y.S. Vergunova, Y. B. Scheck, E. Panina, N. Stepanov, I. Serhiienko, Refractory TaTiNb, TaTiNbZr, and TaTiNbZrX (X= Mo, W) high entropy alloys by combined use of high energy ball milling and spark plasma sintering: structural characterization, mechanical properties, electrical resistivity, and thermal conductivity, *Mater. Sci. Eng., A* 893 (2022) 162030.